Dynamics and stability of an iron drop falling in a magma ocean

B. Qaddah, Julien Monteux, Vincent Clesi, Mohamed Ali Bouhifd, Michael Le Bars

To cite this version:

B. Qaddah, Julien Monteux, Vincent Clesi, Mohamed Ali Bouhifd, Michael Le Bars. Dynamics and stability of an iron drop falling in a magma ocean. Physics of the Earth and Planetary Interiors, 2019, 289, pp.75-89. 10.1016/j.pepi.2019.02.006 . hal-02113925

Dynamics and stability of an iron drop falling in a magma ocean

B. Qaddah[a,b], J. Monteux[a], V. Clesi[a], M.A. Bouhifd[a], M. Le Bars[b]

[a] *Université Clermont Auvergne, CNRS, IRD, OPGC, Laboratoire Magmas et Volcans, F-63000 Clermont-Ferrand, France*
[b] *CNRS, Aix Marseille Univ, Centrale Marseille, IRPHE, Marseille, France.*
Corresponding author: qaddah@irphe.univ-mrs.fr

Abstract

The latest stages of planetary accretion involved large impacts between differentiated bodies, hence large scale melting events. Consequently, the iron brought by the impactors sank within a deep magma ocean, before reaching the protocore. Yet the fluid dynamics of this process remains poorly known. Here, we report numerical simulations of the sinking dynamics of an initially spherical liquid iron drop within a molten silicate phase, up to its possible fragmentation. We consider a 2D cylindrical axisymmetric geometry. We vary the viscosity of the molten silicates in the range of 0.05 Pa.s to 100 Pa.s and the initial radius of the iron drop in the range of 1mm to 350 mm. Hence, we investigate Reynolds number in the range of [0.027 - 85600] and Weber number in the range of [0.073 - 7480]. Our numerical model constrains the morphology, dynamics and stability of the iron drop as a function of the dimensionless Weber and Reynolds numbers as well as of the viscosity ratio between the molten silicates and the liquid iron drop. In particular, we show that the maximal stable drop radius and the critical Weber number are monotonically increasing functions of the magma ocean viscosity. The momentum boundary layer thickness depends mainly on the drop radius and slightly on the magma ocean viscosity. Increasing the viscosity of the silicate phase prevents oscillations of the iron phase and limits the exchange surface. Oppositely, increasing the initial radius of the iron drop enhances its deformation and increases its relative exchange surface. Above the critical Weber number, we confirm that the fragmentation of the liquid iron occurs within a falling distance equal to 3.5-8 times the drop initial radius in the explored range of moderate Weber number, and we describe a variety of fragmentation regimes. Consequences for Earth's formation models are briefly assessed.

Keywords: Core formation, fluid dynamics, numerical modeling, metal drop, magma ocean.

---

1. Introduction

The Earth core formation is a complex process which remains actively debated theoretically, experimentally, and numerically (e.g. Stevenson, 1990; Tonks and Melosh, 1992; Chambers, 2004; O'Brien et al., 2006; Wood et al., 2006; Morbidelli et al., 2012; Deguen et al., 2014; Wacheul et al., 2014; Bouhifd et al., 2017). The core formation is highly dependent on accretion as both processes are contemporaneous (Kleine et al., 2002; Touboul et al., 2007). In the latest stages of planetary accretion, giant impacts have occurred [Fig. 1], leading for instance to the formation of the Moon following the collision between a large differentiated body of Mars size and the proto-Earth (Hartmann and Davis, 1975). The enormous amount of kinetic energy brought in by these collisions (Tonks and Melosh, 1992; Monteux et al., 2007; Samuel, 2012), the decay of short-lived radio-elements (^{26}Al and ^{60}Fe) causing radioactive heating (Walter and Tronnes, 2004), and the heat dissipation from the conversion of potential energy (Monteux et al., 2009; Samuel, 2012) probably led to the formation of deep magma oceans (Tonks and Melosh, 1992). Following the impact, the liquid iron from the impactor core spread and then sank into this less dense magma ocean as an immiscible fluid, leading to thermo-chemical exchanges between the two phases, before merging with the proto-core. This dynamical process may involve deformation of the initial drops coming from the primary breakup at impact, and possibly their breakup into even smaller droplets [Fig. 1] (Samuel, 2012).

Three scenarios have been proposed to characterise the motion of liquid iron within the magma ocean and the thermo-chemical equilibration between the two phases. In the first scenario, i.e. the so-called iron rain model (Stevenson, 1990; Karato and Murthy, 1997; Rubie et al., 2003), it is suggested that an impactor's core with a diameter of $[10-100]$ km immediately fragments into small droplets with a single characteristic diameter of the order of 1cm, corresponding to the capillary size. All droplets descend independently towards the bottom of the magma ocean at the same velocity and without any further change in shape, leading to an efficient chemical equilibration at a distance of less than 200m within the magma ocean. In contrast, Dahl and Stevenson (2010) proposed a theoretical model where the large liquid iron impactor's core does not break up into the magma ocean if its initial size is large enough; it is only eroded by Rayleigh-Taylor and Kelvin-Helmholtz instabilities. Such a core formation episode would be far from thermo-chemical equilibrium between the impactor's core and the magma ocean. More recently, Deguen et al. (2011, 2014) used fluid dynamics experiments to show that a large core always breaks and forms a cloud of droplets with different sizes. But before doing so, it first evolves from its initial state as a turbulent thermal with strong entrainment and mixing, leading to rapid equilibration even before fragmentation.

In these previous studies, the influence of the viscosity ratio between the molten silicates and the liquid iron is neglected. Wacheul et al. (2014) developed analog experiments using gallium to mimic the liquid iron and a mixture of water and glycerol to mimic molten silicates. They found that the value of the viscosity ratio is very important and changes significantly the flow morphology. Later on, Wacheul and Le Bars (2018) validated the turbulent thermal model proposed by Deguen et al. (2014) using global temperature measurements of the liquid metal equilibration. However, numerous questions remain regarding the local dynamics at the scale of one drop, including: What is the maximum stable size of a drop as a function of the viscosity ratio? How is the exchange surface between iron drops and molten silicates influenced by the viscosity ratio? What is the size of the dynamical boundary layer across which the thermal and chemical exchanges occur? Answering those questions is fundamental for a better estimate of the equilibration length in planets, hence for relevant models of planet initial thermochemical state.

Several works have already investigated the dynamics of a buoyant bubble or drop in a viscous environment. For instance, a seminal experimental study of rising bubbles of hydrogen in aqueous sugar solutions is reported by Bhaga and Weber (1981) to determine the shape of the bubble, its terminal velocity, the geometry of its wake, and the flow streamline around it. Several experimental investigations of drop breakup in gas-liquid and liquid-liquid systems are reviewed by Pilch and Erdman (1987). An axisymmetric numerical model of a secondary breakup of a spherical liquid drop falling from rest due to gravity in another immiscible liquid is presented in Han and Tryggvason (1999) for different density and viscosity ratios, showing large drop deformation and various breakup modes. Another axisymmetric numerical investigation of the evolution of a large bubble rising by buoyancy in the presence of both capillary and viscous effects was carried out by Bonometti and Magnaudet (2006), in particular to determine the transition from a spherical cap to a toroidal shape. The influence of viscosity and density ratios is investigated systematically by Ohta et al. (2009, 2010, 2014); Ohta and Sussman (2012). Finally, the first systematics on the asymmetric motion and the fragmentation modes of a bubble of gas rising in a liquid using three-dimensional numerical simulations are reported in Tripathi et al. (2015). However, previous works on the effects of viscosity contrast were motivated by industrial applications mainly, apart from 2 cases in Ichikawa et al. (2010) exploring the relative dynamical changes for viscosity ratios 0.1 and 10 between iron and a magma ocean. In the context of the core formation, the viscosity of the magma ocean strongly depends on its evolving temperature and pressure (Karki and Stixrude, 2010). Hence, the viscosity contrast between the metallic and silicate phases can differ by several orders of magnitude. We thus propose here to constrain the influence of the viscosity contrast between the metallic phase and the magma ocean focusing on the sinking of an unique iron droplet. We also investigate the influence of the droplet radius and derive scaling laws to characterise this fluid dynamics.

The study is organised as follows. Section 2 introduces the physical and numerical model, including the governing equations, the relevant non-dimensional parameters, the numerical model description, and our computational domain and mesh. Section 3 then presents our main numerical results including systematic studies of the drag coefficient, fragmentation modes, characteristic time and distance before breakup, and maximum stable radius before breakup. In Section 4, we discuss possible planetary applications, focusing on the potential efficiency of thermo-chemical exchanges around the drop which depends on the boundary layer thickness and the exchange surface between iron drop and molten silicates. Conclusions and future works are detailed in the final Section 5.

2. Physical and numerical model

2.1. Governing equations

We consider the sinking dynamics of an initially spherical iron drop, falling in a less dense and more viscous fluid under the action of gravity. We assume that both the liquid iron drop and the surrounding molten silicates behave as Newtonian, incompressible, and immiscible fluids with uniform surface tension, and constant density and viscosity within each fluid. We note here that we do not consider the thermo-chemical exchanges that may occur between the two phases. This point will be the subject of a separated study. Hence, the fluid dynamics is governed by the Navier-Stokes equations to characterize:

1. the conservation of mass

$$\boldsymbol{\nabla}.\boldsymbol{u} = 0, \tag{1}$$

2. the conservation of momentum

$$\rho(\frac{\partial \boldsymbol{u}}{\partial t} + \boldsymbol{u}.\nabla \boldsymbol{u}) = \boldsymbol{\nabla}.[-P\boldsymbol{I} + \mu(\nabla \boldsymbol{u} + (\nabla \boldsymbol{u})^T)] + \rho \boldsymbol{g} + \boldsymbol{F}_{st} \tag{2}$$

   with $\boldsymbol{u}$ the fluid velocity vector (m/s), ρ the fluid density (kg/m^3), μ the fluid viscosity (Pa.s), t the time (s), P the fluid pressure (Pa), $\boldsymbol{g}$ the gravitational acceleration (m/s^2), $\boldsymbol{F}_{st}$ the surface tension force (N/m^3) and $\boldsymbol{I}$ the identity matrix.

We monitor the interface between the liquid iron drop and the molten silicates using the Level Set method, an Eulerian and implicit method frequently used in multiphase flow problems (e.g. Luo et al., 2006). It consists in defining a level set function ϕ, equal to 1 in iron and 0 in the surrounding silicates, and rapidly changing through the interface, whose position is determined by the isocontour $\phi = 0.5$. The equation governing the transport and reinitialization of ϕ is :

$$\frac{\partial \phi}{\partial t} + \boldsymbol{u}.\nabla \phi = \gamma \nabla.[\epsilon \nabla \phi - \phi(1-\phi)\frac{\nabla \phi}{\mid \nabla \phi \mid}] \tag{3}$$

with γ (m/s) and ϵ (m) the reinitialization parameters. ϵ determines the thickness of the layer around the interface, and is typically chosen equal to half the size of the characteristic mesh in the region explored by the interface. γ determines the amount of reinitialization: a suitable value for γ is the maximum velocity magnitude experienced in the model.

The density and dynamical viscosity are evaluated using the level set function:

$$\rho = \rho_s + (\rho_d - \rho_s)\phi \tag{4}$$

$$\mu = \mu_s + (\mu_d - \mu_s)\phi \tag{5}$$

where subscripts “s” and “d” stand for the molten silicates and the liquid iron drop respectively.

The surface tension force is determined by :

$$\boldsymbol{F}_{st} = \nabla.\boldsymbol{T} = \nabla.(\sigma[\boldsymbol{I} + (-\boldsymbol{n}\boldsymbol{n}^T)]\delta) \tag{6}$$

with σ (N/m) the surface tension coefficient, I the identity matrix, $\boldsymbol{n}$ the interface normal unit vector, and δ the Dirac delta function, nonzero only at the fluid interface. The interface normal unit vector is calculated as

$$\boldsymbol{n} = \frac{\nabla\phi}{\mid \nabla\phi \mid}. \tag{7}$$

The level set parameter ϕ is also used to approximate the delta function by a smooth function (Hu et al., 2014) defined by

$$\delta = 6 \mid \phi(1-\phi) \mid\mid \nabla\phi \mid . \tag{8}$$

2.2. *Physical and non-dimensional parameters*

According to the Buckingham Π theorem, in our study, there are 6 dimensionless numbers based on the control parameters (see Figures 1 and 2). One could for instance choose the two aspect ratios related to the drop vs. the computational domain sizes, the density ratio, the viscosity ratio, and then define *a priori* Weber and Reynolds numbers based on the Newton theoretical velocity (see e.g. Wacheul et al., 2014). A complete dynamical study would then necessitate to explore the influence of those 4 later parameters in a computational box sufficiently large such that boundary conditions do not influence the dynamics. Here, we are interested in determining the dynamics of metal drops sinking into a magma ocean: we thus vary only the drop radius and the magma ocean viscosity, which are the main variables in the geophysical situation of interest, while we keep all the other dimensioned parameters fixed at their expected geophysical values (see Table 1).

In each simulation, starting from rest, the drop accelerates until reaching a constant terminal velocity, possibly with small oscillations around it. We monitor this mean terminal velocity V for each case. We end up our simulations when either the drop reaches a stable regime before the bottom of the domain or the drop fragments. In the later case the axisymmetric approximation is not relevant anymore. Each run is thus characterised by the 4 dimensionless numbers:

- the Reynolds number compares inertia and viscous effects : $Re = \frac{\rho_s V D}{\mu_s}$, with $D = 2R$ the drop initial diameter (R is the initial radius). The Reynolds number determines the falling drop dynamical regime : $Re < 1$ implies a Stokes regime where the viscous effects dominate; $Re = 1 - 500$ implies an intermediate regime where both viscous effects and inertial forces are important; and $Re > 500$ implies a Newtonian regime where the inertial forces are dominant (see Samuel, 2012).

- the Weber number measures the relative importance of inertia over surface tension: $We = \frac{\rho_s V^2 D}{\sigma}$. It controls and governs the deformation and breakup of the drop (Pilch and Erdman, 1987). Indeed inertia forces aim at deforming and fragmenting the iron drop, while the surface tension force prevents it from deformation and disruption. When $We \gg 1$, the inertia forces dominate leading to strong deformation and rapid fragmentation (e.g. Wacheul et al., 2014).

- the viscosity ratio is defined as the ratio of the silicates viscosity over the iron drop viscosity: $R_\mu = \frac{\mu_s}{\mu_d}$. The viscosity of liquid iron weakly depends on pressure and $\sim 5 \times 10^{-3}$ Pa.s at both inner core boundary pressure conditions (Poirier, 1988) and at the Earth surface (Assael et al., 2006). Oppositely, the magma ocean viscosity varies between 10^{-4} and 100 Pa.s depending on the thermal and dynamic conditions (Karki and Stixrude, 2010; Rubie et al., 2003; Samuel, 2012). In our model, we fix the viscosity of the metallic phase and the viscosity contrast ranges between 10 and 20000.

- the density ratio compares the iron drop density over the silicates density: $R_\rho = \frac{\rho_d}{\rho_s}$. The densities of liquid iron and molten silicates depend on the temperature and pressure conditions (Assael et al., 2006; de Wijs et al., 1998; Samuel, 2012). In our models, for simplicity, we fix $\rho_d = 7500$ kg.m^{-3} and $\rho_s = 3500$ kg.m^{-3}. As a consequence, in this study, the density ratio is constant and equals to 2.14.

After a large collision involving two differentiated protoplanets, the core of the impactor is first fragmented in large scale iron structures (Kendall and Melosh, 2016). In the magma ocean, these structures overcome a second fragmentation resulting in the formation of a cloud of droplets with typical size ranging between a few millimetres to several centimetres (Deguen et al., 2014; Wacheul et al., 2014). In our study, we characterize the dynamics of a droplet in the iron cloud and determine the influence of the viscosity contrast on this droplet. For that, we vary the initial radius of the drop from 1 to 350 mm, exploring a large range of expected sizes in the iron rain cloud.

All the parameters used in this paper are listed in Table 1.

Table 1: Symbol definitions and values of the physical and non-dimensional parameters used in this study. Reynolds and Weber numbers are defined *a posteriori* using the relevant terminal velocity, measured in each run.

	Symbol	Value or range
Silicates density	ρ_s	3500 kg/m^3
Iron drop density	ρ_d	7500 kg/m^3
Density ratio	R_ρ	2.14
Iron drop viscosity	μ_d	0.005 Pa.s
Magma ocean viscosity	μ_s	0.05 - 100 Pa.s
Viscosity ratio	R_μ	10 - 20000
Initial drop radius	R	1 - 350 mm
Surface tension coefficient	σ	1 N/m
Reynolds number	Re	0.027 - 85600
Weber number	We	0.073 - 7480

2.3. Numerical method

In this work, we solve equations (1 - 3) using the COMSOL Multiphysics software, based on the finite element method. We study a 2D axisymmetric geometry with no-slip boundary conditions at the lateral boundary and open boundary conditions at the top and bottom boundaries. To avoid the wall effects, the computational domain must be large enough. For instance, Bonometti and Magnaudet (2006) considered a computational domain of $5.5D \times 12.6D$ to avoid contamination of the results. Their computations are stopped before the bubble arrives too close to the domain boundary. Ohta et al. (2010) used a computational domain of $4D \times 6D$, and considered a levitating drop with an entering inflow at the top boundary equal to its terminal velocity. Samuel (2012) also considered a levitating drop but with a square computational domain of $5D \times 5D$, and the inflow velocity is self-adjusting at the instantaneous velocity of the center of mass of the drop. Here, we have checked the convergence of our results as a function of the domain size, and we do not see any significant difference once the domain is larger than $4D$ and longer than $75D$. As sketched in figures 1 and 2, our computational domain is an axisymmetric cylinder of size $(r \times z) = (6D \times 100D)$.

The drop dynamics requires a fine mesh to capture all its details while conserving the overall mass of iron. Especially, the level set method has a tendancy to diffuse numerical artifacts on the interface and then gives incorrect results. Since our computational domain is very large, we need an adaptive mesh strongly refined in the drop vicinity, which we have implemented manually. To do so, we divide our domain in several regions, as shown in figure 2. We mesh the region that the drop crosses over a given time interval with a very fine mesh of size $h_x = 0.025R$, small enough to capture all the dynamics on the interface without any significant error or numerical diffusion. We mesh the region behind the drop with a thin mesh $h_x = 0.07R$ to correctly capture the physics of the wake, which also influences the dynamics. The mesh around the drop gradually widens in the radial direction until reaching $h_x = 0.2R$, from where it remains fixed until the wall. Finally, our mesh in front of the drop in the vertical direction first increases in an intermediate region to $h_x = 0.07R$, and then keeps increasing until reaching a very large value $h_x = 5000R$. When the drop approaches the bottom of the finer mesh region, the simulation is stopped, the whole pattern is translated, and the simulation is restarted on this new grid. We have tested this procedure and found that the dynamics of the falling drop doesn't change significantly when using smaller h_x (see Appendix). Also the overall iron mass during the course of each complete computation does not change by more than 0.7%, hence showing good numerical convergence. This method is relatively inexpensive in term of calculation time, and allows for a systematic study, with runs taking from 7 hours to one week on a bi-processor, $3.2-3.6$ GHZ, computer.

Table 2: Non-dimensional parameters for all performed simulations used in this study. In all our simulations, $R_\rho = 2.14$.

Simulation	Re	We	R_μ	$R(mm)$
#1	19.7	0.139	10	1
#2	315	7.09	10	5
#3	372	8.22	10	6
#4	426	9.27	10	7
#5	553	10.9	10	10
#6	1610	37.0	10	25
#7	3280	95.8	10	40
#8	73.9	8.13	50	6
#9	93.0	9.64	50	8
#10	106	11.1	50	9
#11	108	10.4	50	10
#12	202	24.2	50	15
#13	322	37.0	50	25
#14	638	91.0	50	40
#15	1510	290	50	70
#16	14.3	1.82	100	6
#17	35.3	7.43	100	8
#18	44.2	8.74	100	10
#19	51.8	9.58	100	11
#20	66.0	13.5	100	11.5
#21	71.4	15.2	100	12
#22	92.4	20.3	100	15
#23	154	33.9	100	25
#24	314	87.8	100	40
#25	750	287	100	70
#26	11.9	3.35	200	6
#27	19.7	6.90	200	8
#28	25.1	9.02	200	10
#29	30.4	11.0	200	12
#30	36.4	14.6	200	13
#31	38.7	15.3	200	14
#32	42.5	17.2	200	15
#33	76.1	33.1	200	25
#34	146	75.7	200	40
#35	363	268	200	70
#36	637	580	200	100
#37	1.53	1.05	1000	8

Simulation	Re	We	R_μ	$R(mm)$
#38	2.70	2.61	1000	10
#39	6.49	10.0	1000	15
#40	11.2	22.4	1000	20
#41	15.4	33.9	1000	25
#42	19.7	46.4	1000	30
#43	26.0	68.8	1000	35
#44	28.8	74.3	1000	40
#45	38.5	106	1000	50
#46	52.1	161	1000	60
#47	68.6	240	1000	70
#48	122	530	1000	100
#49	0.027	0.073	20000	15
#50	0.127	0.927	20000	25
#51	0.509	9.27	20000	40
#52	0.952	25.9	20000	50
#53	1.22	38.7	20000	55
#54	1.54	56.6	20000	60
#55	2.27	105	20000	70
#56	5.15	379	20000	100
#57	24.4	26.5	500	20
#58	7.56	42.5	2500	30
#59	8.42	49.5	2500	35
#60	9.82	61.2	2500	40
#61	12.3	84.7	2500	45
#62	2670	636	50	100
#63	24100	1380	10	150
#64	37100	2460	10	200
#65	67800	5480	10	300
#66	85600	7480	10	350
#67	4770	1350	50	150
#68	7360	2420	50	200
#69	13400	5380	50	300
#70	16960	7330	50	350
#71	2380	1350	100	150
#72	3660	2400	100	200
#73	6700	5340	100	300
#74	8430	7290	100	350
#75	1180	1330	200	150
#76	1820	2370	200	200
#77	3360	5360	200	300

Simulation	Re	We	R_μ	$R(mm)$
#78	4221.35	7273.386	200	350
#79	231	1270.5	1000	150
#80	502.25	3603.643	1000	250
#81	667.8	5309.01	1000	300
#82	837.9	7164.045	1000	350
#83	28.35	17.22	300	15
#84	24.57	19.2	400	18

3. Systematic numerical study

We performed 84 simulations, whose dimensionless parameters are given in Table 2. In the following sections, we discuss our obtained numerical results in terms of drag coefficient, fragmentation modes, time and distance before breakup, and maximum stable drop radius. A particular attention is paid to the influence of the viscosity contrast between the metallic and silicate phases. The influence of the initial drop shape is shortly addressed at the end of this section; everywhere else, we start from a spherical drop.

3.1. Drag coefficient

The drag coefficient is a dimensionless number that quantifies the drag or resistance of the sinking drop into the magma ocean. It strongly depends on the viscosity ratio, density ratio, and surface tension, all of which control the interface conditions. In our case where the driving force is buoyancy and the initial geometry is spherical, we classically define the drag coefficient as

$$C_D = \frac{8}{3}\frac{(\rho_d - \rho_s)gR}{\rho_s V^2}, \tag{9}$$

with V the measured terminal velocity. Below, we first rapidly review the different theroretical models for the drag coefficient, and then compare with our numerical measurements.

3.1.1. *For small Reynolds numbers*

Several previous studies focused on the analytical determination of the drag coefficient for spherical fluid particles (e.g. Clift and Gauvin, 1970; Hadamard, 1911; Mei et al., 1994) and for deformed fluid particles (e.g. Moore, 1965; Darton and Harrison, 1974; Clift et al., 1978; Loth, 2008). For spherical drops, the internal circulation is supposed to prevent forming any wake separation of the external flow. This in turn helps to prevent any change in shape and keeps the droplet spherical. Hadamard (1911) proposed an analytical relation at finite but low Reynolds $Re \ll 1$. An asymptotic solution was derived by Harper and Moore (1968) for intermediate Reynolds numbers but remains limited to $Re < 100$ at finite values of the viscosity ratio. To fill the gap between Harper and Moore (1968) and Hadamard (1911), an empirical mixed Stokes correction factor resulting from the internal circulation was proposed by Mei et al. (1994) in the limit $R_\mu \to 0$:

$$C_{D_{R_\mu \to 0}} = \frac{16}{Re}[1 + [\frac{8}{Re} + \frac{1}{2}(1 + \frac{3.315}{\sqrt{Re}})]^{-1}]. \qquad (10)$$

3.1.2. *For moderate and large Reynolds numbers*

For intermediate but increasing Reynolds numbers ($0.1 < Re < 2000$), the drop begins to distort, leading to changes in the wake from an attached laminar wake (spherical drop), to a separated laminar wake (deformable drop), to an unsteady transitional wake (breakup into droplets) and finally to a turbulent wake (catastrophic breakup) (Loth, 2008). The wake actually depends on the interplay between surface tension and hydrodynamic pressure stresses, hence on We. Davies and Taylor (1950) found a converged value $C_D = \frac{8}{3}$ for gas bubbles in a liquid at infinite Reynolds and Weber numbers. In order to encompass the influence of viscosity and a wide range of small to large Reynolds numbers, an empirical correlation was proposed by Darton and Harrison (1974) and Clift et al. (1978) for infinitely large We:

$$C_{D_{We\to\infty}} = \frac{8}{3} + \frac{24}{Re}(\frac{2+3R_\mu}{3+3R_\mu}). \tag{11}$$

To capture the drag in the intermediate range of Re and We values (of interest here), Loth (2008) proposed the following expression by combining Eqs.10 and 11 and adding a functional dependence ($\Delta(C_D)^*$) on We, where $\Delta(C_D)^*$ increases monotonically with Weber number:

$$C_D = C_{D_{We\to 0}} + \Delta(C_D)^*[C_{D_{We\to\infty}} - C_{D_{We\to 0}}] \tag{12}$$

$$\Delta(C_D)^* = \tanh(0.021We^{1.6}). \tag{13}$$

Here $C_{D_{We\to 0}}$ is given by Eq.10, the imposed spherical shape being related to an infinite surface tension, hence to $We \to 0$. Experimentally, several investigations partly tackled the relevant limit of a metal drop in a more viscous environment, including: the fragmentation of liquid mercury drops sinking within water reported by Patel (1978); Patel and Theofanous (1981), who found a drag coefficient equal to $2.5 - 3$; the fragmentation of gallium drops in water by Kim et al. (1983), who found that the drag coefficient depends on the Reynolds number; and the analog model of Wacheul and Le Bars (2018), who reported a convergence value of the drag coefficient at large Reynolds equal to 3.7 ± 1.

3.1.3. Results and discussion

We have monitored the velocity V of the sinking metallic drop in our simulations and obtained the corresponding values for C_D from Eq.9. Figure 3 presents our measured C_D as a function of the Reynolds number for various viscosity ratios, and the comparison of our results with the analytical solutions of Mei et al. (1994) (Eq. 10) and Loth (2008) (Eq. 12) . For $We < 1$ and low Reynolds numbers (up to $Re = 20$ depending on R_μ), the droplet remains spherical and our results agree with the analytical model proposed by Mei et al. (1994): C_D is inversely proportional to Re and barely depends on the viscosity ratio. When flow separation occurs (i.e. when the Weber number exceeds unity), this expression is not valid anymore because the drop deforms: it takes the shape of an ellipsoid, a disc or a cup. This deformation increases the frontal area and leads to a transient increase of C_D with Re, depending on R_μ. Qualitative agreement between our simulations and Eq.12 is satisfactory, but small quantitative differences exist. This is not surprising, since the empirical formula Eq.12 was calibrated on gas bubbles rising in a liquid, which are more sensitive to deformation than the liquid drops studied here. But no equivalent to Eq.12 is yet available for liquid-liquid systems, and one has thus to rely on numerical results. Finally, for large Re, C_D converges towards a constant value 3.5 ± 0.5, independtly of R_μ. This value is above the analytical estimate of $8/3$, but is compatible with the results of Wacheul and Le Bars (2018) who found a mean value of C_D equal to 3.7 ± 1.

3.2. Fragmentation modes

The breakup mechanism is very sensitive to the Weber number, as well as to the viscosity ratio between the metal and the silicates. Two main fragmentation modes have been documented in previous experimental and numerical studies, namely the "bag breakup" just above the critical Weber number, and the "shear breakup" at large Weber number (see the limit cases in Fig. 4) (Krzeczkowski, 1980; Pilch and Erdman, 1987; Dai and Faeth, 2001). Several authors have tackled the description of the different breakup mechanisms in the intermediate range of Weber number, leading to a complex situation. Examples include Krzeczkowski (1980), who developed series of experiments for liquid droplets of water, methanol, ethanol, butanol and glycerine in an external air stream, and documented two breakup modes independent of the viscosity ratio: the "bag-jet" and the "transition" modes. Pilch and Erdman (1987) introduced two breakup modes for a single liquid drop within an external gas flow: the "bag-stamen" mode and the "sheet stripping" mode. Dai and Faeth (2001) used droplets of water and ethanol and defined a "bag-plume" mode, close to the "bag-jet" and "bag-stamen", and a "plume-shear" mode, close to the "shear breakup". Cao et al. (2007) pursued this experimental investigation and presented a new "dual-bag" breakup mode for $We = 28 - 41$. Recently, $3D$ numerical simulations of liquid droplets levitating in a gas flow with a uniform velocity have been performed by Kékesi et al. (2014), changing the viscosity and density ratios for a fixed Weber number value ($We = 20$). They identified 5 breakup regimes, as shown in Fig. 4: "thick rim shear" and "thick rim bag" (both close to "bag breakup"), "rim shear", "jellyfish shear", and "shear" breakup respectively. In our study, we use their classification.

For each mode of fragmentation, we describe below the temporal evolution of a typical spherical drop starting from rest at $t = 0$, until its breakup at $t = t_{bk}$.

- Thick rim shear (Fig. 5): the initial sphere rapidly deforms into a spherical cap ($t = 0.13$s), then the hydrodynamic pressure force concentrates on the middle of the drop leading to the formation of a small bag ($t = 0.2$s). Surface tension then prevents breakup and the drop returns to form a half-sphere ($t = 0.355$s), before a second oscillation starts. Then, as the inertial forces and associated pressure are reinforced, the vertical thickness decreases even more, and a thin film forms near the symmetry axis, with a thicker rim ($t = 0.55$s). The rim extends radially and drains out the liquid film ($t = 0.6$s), until a hole occurs at the symmetry axis ($t = 0.62$s). At this stage, the metal phase actually forms a ring that might persist for a longer time before fragmentation of Rayleigh-Plateau type, to which we cannot have access with our axisymmetic simulation. Kékesi et al. (2014) showed in 3D simulations that this last stage is actually rapid, i.e. a few milliseconds. Note also that thick rim shear seems marginal in the parameter space explored here, and is replaced rapidly by thick rim bag, except for cases with the smaller viscosity ratio $R_\mu = 10$ (see Fig. 4).

- Thick rim bag (Fig. 6): this breakup process is similar to the thick rim shear, until fragmentation. Then, breakup appears almost simultaneously in the center of the drop ($t = 0.675$s) and at the connection between the film and the rim, forming satellite droplets ($t = 0.68$s).

- Rim shear (Fig. 7): again the initiation of the breakup is similar to the two processes described above, with the formation of a spherical cap ($t = 0.131$s), followed by a bag ($t = 0.2$s), and back ($t = 0.37$s). Then, the drop extends in both radial and vertical directions, forming a sheet ($t = 0.48$s and 0.51s) under the action of the strong vorticity in the wake. Finally, surface tension drains the iron both into the center and into the rim ($t = 0.57$s), while the sheet connecting the two thins, and finally breaks ($t = 0.59$s).

- Jellyfish shear (Fig. 8): in this mode, no rim forms. Instead, a thin skirt forms while iron is mostly localized along the symmetry axis ($t = 0.4$s and $t = 0.45$s). Oscillations develop in the thin membrane, whose ends fold in and out. The velocity is concentrated in the wake of the silicates which accelerates the drop center relative to its membranes, leading to a rapid fragmentation in the connecting region ($t = 0.51$s).

- Shear breakup (Fig. 9): the drop shape deforms first into a spherical cap ($t = 0.24$s) and second into a skirt. Then, the rim does not thicken,

> but folds inside and turns around itself through the action of vorticity, leading to its thinning ($t = 0.4$s). Rapidly, this thin sheet breaks into small droplets ($t = 0.42$s). No oscillations are observed here, and the rapid fragmentation is mainly due to the vorticity in the wake behind the drop that is two to three times larger than the vorticity in the drop.

The deformation of the droplet depends on the viscosity of the external flow, the density ratio, the surface tension and the drop size. When Re and We are both small, the drop remains spherical without any deformation, due to the internal circulation within the drop that prevents forming any separated wake. When the hydrodynamic pressure force increases, a separated laminar wake and an external circulation behind the drop occur, leading to shape deformation. Increasing the Reynolds number, the drop first deforms to an ellipsoid, and possibly gives rise to oscillations from oblate to prolate shapes. For a viscosity ratio less than 100, the drop keeps oscillating until the end of the domain, while for a viscosity ratio greater than 100, the velocity of the drop exceeds the oscillation velocity, leading to rapid damping of the initially excited oscillation. Further increasing the Reynolds number, the drop takes the shape of a spherical cap. And once hydrodynamic pressure overcomes surface tension (i.e. large enough Weber number), one of the five fragmentation modes occurs, depending also on the viscosity ratio. From our systematic study for different viscosity ratios, we built up a fragmentation regime diagram in terms of Reynolds and Weber numbers shown in Fig. 4. For a viscosity ratio $R_\mu = 1000$, we observe only two modes, and drop oscillations are prevented by the high silicates viscosity. On the contrary for $R_\mu = 50$, we observe the five different modes and strong drop oscillations. One should also notice that the critical Weber number depends on the viscosity ratio: for $R_\mu = 10$, the breakup begins at $We \approx 9$ while for $R_\mu = 1000$, it starts at $We \approx 34$. Systematic estimate of the critical

Weber number is shown in Fig. 10. We consider in this figure that fragmentation occurs as soon as the first volume of iron separates from the main drop. The increase in the viscosity ratio leads to an increase in the critical Weber number following two empirical scaling laws depending on first-breakup regime. When the viscosity ratio is rather low (i.e. < 300 typically), the drop fragments quickly as a thick rim shear after only one or two oscillations along a short drop path. In this case, critical Weber is defined as a low power law of the viscosity ratio by the following scaling law

$$We_c = 5.7 R_\mu^{0.187}. \tag{14}$$

On the other hand, at a viscosity ratio of ~ 300, a Jellyfish behaviour takes place, and between $R_\mu = 300$ and $R_\mu = 500$, the drop first breakup becomes slow and transitions from thick rim shear to Jellyfish. In this region and above, where shear breakup takes place, the critical Weber number depends more significantly on the viscosity ratio and is given by the following scalling law

$$We_c = 1.137 R_\mu^{0.483}, \tag{15}$$

valid at least in the range $R_\mu = [300; 2500]$ explored here.

From our simulation #41, we also report a new fragmentation mode illustrated in Fig. 11. This mode is initially similar to the jellyfish shear breakup except that the membrane fold is so important that it finally closes at the back, encapsulating the silicates within a bubble of iron (Fig. 11, $t = 3.7$s). Then, the next oscillation of the membrane tears the glued back which breaks from the center, forming one central droplet and two satellites droplets. Note that Wacheul et al. (2014) observed in their experiments similar bubbles of metal enclosing the viscous ambiant fluid and exhibiting a lower velocity that pure iron droplets. While being dynamically intriguing, this mode remains very marginal.

3.3. Time and distance before breakup

After an impact, large drops deform and fragment at a distance and time that depend on the sinking dynamics. We define these time and distance as the breakup time t_{bk} and distance d_{bk}. Deguen et al. (2014) predicted that for large Weber numbers, t_{bk} and d_{bk} reach an asymptotic regime. In this section we test this prediction. From our models, we determine t_{bk} and d_{bk} as the time and location where the first droplet or ligament of iron separates from the main drop. We then define the dimensionless breakup time t^*_{bk} as Pilch and Erdman (1987):

$$t^*_{bk} = \frac{t_{bk} V}{D} \sqrt{\frac{\rho_d}{\rho_s}} \tag{16}$$

where the break up time is normalized by the characteristic time of drop breakup by Kelvin-Helmholtz instability. We define the dimensionless breakup distance as:

$$d^*_{bk} = \frac{d_{bk}}{R}. \tag{17}$$

Fig. 12 shows the variations of t^*_{bk} as a function of the Weber number for various viscosity ratios. From Fig. 12, we see that t^*_{bk} decreases with the increase of We. We note that, for large We, t^*_{bk} converges towards a constant value ranging between 1 and 1.8. This result is consistent with the result of Pilch and Erdman (1987) who found $t^*_{bk} = 1.25$ for $We > 350$. A dependence on the viscosity ratio is also present, especially at $We \leq 80$, with a tendency for large R_μ to stabilise the drops.

The non-dimensionalised breakup distance d^*_{bk} is reported in Fig. 13. It also shows a dependence on the viscosity ratio, especially at low We, and a possible convergence towards an asymptotic value ranging between 2 and 4 at large We. For comparison, Deguen et al. (2014) found a breakup distance equal to $6-8$ times the drop radius for We up to 3000 and $R_\mu = 0.5$. Landeau et al. (2014) found a value equal to $3.5-7.5$ times the radius for $25 < We < 1000$ and $0.45 < R_\mu < 1.25$. Hence our results are in correct agreement with those experimental observations. This is all the more noticeable that Landeau et al. (2014) observed 3D turbulence in lab experiments at $We > 600$, effects that are missing from our axisymmetric simulations. Note finally that Wacheul and Le Bars (2018) found a breakup distance $(13 \pm 2)R$ for $10 < We < 50$ and $0.4 < R_\mu < 700$, but their breakup criteria actually detected a "significant" and well-advanced breakup, thus implicitly leading to an overestimation of d^*_{bk} compared to other results. Figure 13 illustrates the influence of the viscosity ratio on the breakup distance. For low We, d^*_{bk} ranges between 10 and 80 for the whole range of viscosity ratios used in our study. For large We, d^*_{bk} ranges between 2 and 4.5. Increasing the viscosity ratio generically increases the breakup distance and as a consequence, the potential depth of equilibrium between iron drops and silicates.

3.4. Maximum stable drop radius

After an impact, the impactor's iron core disrupts into large scale drops (Kendall and Melosh, 2016). After this first fragmentation, a second fragmentation occurs within the magma ocean resulting in the formation of a cloud of droplets (Deguen et al., 2014; Wacheul et al., 2014). At the end of this second fragmentation, iron droplets reach a maximum stable radius R_{max}. Following Wacheul et al. (2014) and using the Newtonian velocity scale accounting for the drag coefficient (Eq.9), R_{max} is simply related to the critical Weber number by

$$R_{max} = \sqrt{We_c \frac{3C_D}{16} \frac{\sigma}{\Delta\rho g}}. \tag{18}$$

Numerical data from Fig. 14 show the last drop radius for which deformation may occur but without fragmentation. According to Fig. 14, the maximal stable drop radius increases with the magma ocean viscosity. From our numerical data, we propose a scaling law to determine the maximum stable radius as a power function of magma ocean viscosity, valid for magma viscosities larger than ~ 0.1 Pa.s up to 100 Pa.s :

$$R_{max} = 0.014 \mu_s^{0.32} (m). \tag{19}$$

Our results are in agreement with the analytical Eq. 18, confirming the self-consistency of our numerical results. Fig. 14 also shows the comparison of our results with the model of Rubie et al. (2003) and the model of Samuel (2012). Differences come from different values of C_D, where we use our effective numerical values rather than any theoretical estimation. It should also be noted that Rubie et al. (2003); Samuel (2012) do not consider the dynamical influence of the viscosity contrast between metal and silicates in their models.

3.5. The influence of initial conditions

After an impact, the impactor's core is likely fragmented in metallic diapirs with a large range of shapes (spherical, oblate or prolate) (Kendall and Melosh, 2016). This deformation process is likely to affect the post-impact sinking dynamics of the metallic phase as we envision in our study by modifying our initial shape conditions. Bonometti and Magnaudet (2006) found that their final bubble topology and features vary with the initial shape of the bubble. Without trying to be exhaustive on this subject that would deserve a dedicated study on its own, we have thus investigated the behavior of a drop at the critical Weber number for two viscosity ratios ($R_\mu = 200$ and $R_\mu = 1000$), starting from a spherical, oblate or prolate form with an ellipticity ranging between 0.59 and 0.82, maintaining the total volume of iron constant. Results for $R_\mu = 1000$ are shown in Fig. 15, reporting a significant sensitivity to initial conditions. For the initial oblate form, the drop does not fragment and converges to a skirt shape. On the contrary, the initial prolate shape disrupts more rapidly than the spherical case, the time and distance before breakup being respectively 27.4% and 28.3% smaller than the corresponding values for the spherical case. The shape is also different, with an increase of the surface in the prolate case of 10.9% compared to the spherical case. For the other viscosity ratio $R_\mu = 200$, we find that the fragmentation modes are identical for the three initial conditions, but differences on the order of 10% exist in the breakup time, distance before breakup, and surface. Among the three initial cases, the spherical initial condition always leads to a less rapid fragmentation and to a smaller surface.

4. Implications for the metal/silicate exchanges

In the present study, we focus on the dynamics of the two phase flow only, without considering neither the thermal evolution of the metallic droplet nor chemical exchanges that could occur between the metallic and silicate phases. Our results nevertheless enable to constrain two fundamental parameters for thermochemical equilibration, namely the thickness of the boundary layer at the iron / silicates interface, and the surface of the metallic droplet across which thermochemical exchanges are likely to occur. Those two points are addressed below. We then propose some first order estimates of the equilibration of an initially 10 km metallic core sinking and fragmenting within a magma ocean and compare our results with the classical iron-rain model (Rubie et al., 2003).

4.1. Boundary layer thickness

During the sinking of an iron drop, three boundary layers can form at the interface between the metalic and silicate phases: the dynamical, thermal and chemical boundary layers. The thickness of each boundary layer may have a strong influence on the thermo-chemical exchanges. In this study, we focus on the dynamical boundary layer δ. We thus consider a velocity profile along the normal to the drop interface at the front of the drop, as shown in Fig. [16]: δ is defined as the distance from the drop interface to the point where the velocity is equal to 10% the drop terminal velocity. In the case of a rigid sinking sphere, the thickness of the boundary layer scales as $Re^{-1/2}$ (Ulvrová et al., 2011). In our models, the metallic droplet is deformable and three parameters *a priori* control the flow, hence δ: R_μ, Re and We. Here, we seek a power law for the boundary layer thickness in terms of the two varied parameters in our study, namely the drop radius and the magma ocean viscosity.

Our numerical results are shown in Fig. 17. A good fit is found with the empirical scaling law

$$\delta = 1.442 R^{0.916} \mu_s^{0.062} (m). \tag{20}$$

Hence, the boundary layer thickness depends mainly on the drop radius and only slightly on the magma ocean viscosity. For a standard viscous boundary layer in the vicinity of a solid sphere, one would expect a scaling $\propto \mu_s^{0.5}$. This surprisingly low dependence on the ambient viscosity is probably due to the drop deformation and to the associated internal circulations and wake. It presumably affects the equilibration. Note however that Eq. 20 is valid in the frontal section of the drop, but the boundary layer size is not constant along the drop surface. Also, the generated wake might encapsulate silicates that are entrained with the falling iron, as shown in Fig. 18 and observed numerically (Monteux and Arkani-Hamed (2014)) and experimentally (Fleck et al. (2018)), for an even more viscous surrounding fluid. This also influences equilibration. Clearly, the equilibration process is complex, global, and deserves a study on its own.

4.2. Time evolution of the droplet surface

The exchange surface between two fluids qualifies the surface through which thermo-chemical transfers occur. As shown in the figures 5, 6, 7, 8, 9 and 11, the spherical drop deforms and oscillates during its sinking. This leads to variations in the potential exchange surface between the liquid iron and the molten silicates.

We monitored the surface S of each drop from its initial position until reaching a stationary regime or until breakup. We normalized S by the corresponding spherical surface ($S^* = S/(4\pi R^2)$). Fig. 19 shows the evolution of S^* as a function of time for an initial radius $R = 10$ mm. Fig. 19 illustrates the influence of the viscosity contrast R_μ. For $R_\mu = 1000$, the drop remains spherical and its normalised surface is constant ($S^* = 1$). When the magma ocean viscosity decreases, the deformation of the drop becomes significant and the oscillations of the drop lead to oscillations of its surface. For $R_\mu = 100$, the drop deforms and oscillates several times, but the surface tension is large enough to prevent the drop from breaking up, and a steady state is reached after 1.5s. For $R_\mu = 10$ and $R_\mu = 50$, the drop surface oscillations are followed by a fragmentation (at 0.393s and 0.6s respectively). These large deformation processes significantly increase the droplet surface, which can increase by up to 200% before the fragmentation. Our results show that the viscosity ratio between the liquid iron and silicate phases strongly influences the shape of the metallic drops. As a consequence, considering a purely spherical drop when calculating the transfers across the exchange surface provides only a lower bound estimate which might be significantly off, especially for $R_\mu < 100$.

4.3. Application to a 10 km metal diapir

In the previous sections, we studied the dynamical properties of sinking droplets as a function of the viscosity ratio between the iron droplet and the magma ocean. We showed that, within an iron cloud, each droplet is associated to a boundary layer thickness and an exchange surface that both depend on the droplet size and viscosity ratio. In our numerical models we do not solve the equations governing the thermo-chemical transfers between the metallic droplets and the magma ocean. However, we can estimate the efficiency of the potential thermo-chemical equilibration by determining the total potential exchange surface within a metallic cloud composed of small droplets and resulting from the fragmentation of a 10 km radius metallic diapir, which is the typical lengthscale of iron fragments dispersed after a large impact (Kendall and Melosh, 2016). We consider in these estimations that the 10km metallic diapir is fragmented in a population of small droplets that compose a larger scale metallic cloud sinking through the magma ocean (Deguen et al., 2014).

To characterize the size of the droplets within the cloud, we used the analytical law for the distribution of droplets sizes obtained from the fragmentation of a large analog diapir with a viscosity ratio $R_\mu = 50$ derived experimentally by Wacheul et al. (2014). We assume here that this analytical law is valid for any system with the same viscosity ratio once it is normalised by the characteristic radius of the system, i.e. the maximal stable radius R_{max}. The number of drops $n(R)$ for a given radius R resulting from the breakup of a 10 km iron core is then associated to a gamma distribution:

$$n(R) = NR^{k-1}e^{-\frac{R}{\theta}} \tag{21}$$

where N is a multiplicative constant determined by volume conservation of iron, k is the shape of the gamma distribution, and θ is the scale of the gamma distribution normalised by R_{max}. Wacheul et al. (2014) explicitly mentioned that the shape and scale might depend on the viscosity ratio. In the absence of any further data, we assume constant values with $\theta = 1.9$ and $k = 2.2$ for viscosity ratios ranging between 10 and 1000. Note that R_{max} is nearly constant in the study of Wacheul et al. (2014) and Eq. 21 is obtained from a snapshot at a given time relatively shortly after the primary breakup, where transient large radius drops are still present. In our study, we have shown that R_{max} is a function of the magma ocean viscosity (Fig. 14). Hence, for each magma ocean viscosity, we use R_{max} from our numerical study (Fig. 14) and determine N by volume conservation from a initially 10 km iron diapir radius. We then compute the number of drops of each size, and their relative surface of exchange normalised by their corresponding spherical surface.

We have shown in our numerical models that shape oscillations might influence the surface of the drops (Fig. 19), especially for the largest radii and smallest viscosity ratio. We consider here three models of droplet population within the cloud:

1. a non oscillating population of droplets with a constant radius for a fixed viscosity corresponding to the classical iron rain scenario (Rubie et al., 2003),
2. a non oscillating droplet population derived from our models with variable radii where the droplets remain spherical,
3. an oscillating population derived from our models with variable radii where the droplets deform.

Fig. 20 shows the total dimensionless surface within the fragmenting cloud for the three different cases. In all cases, the exchange surface decreases when increasing the magma ocean viscosity because the maximum stable drop radius also increases when increasing the magma ocean viscosity (see Fig. 14). In the iron rain scenario, the population is composed of droplets smaller than in the two cases derived from our models (oscillating and non oscillating) where large drops are allowed in the distribution. Hence the potential exchange surface is larger (up to 60%) in the iron rain scenario and the equilibration should be more efficient. For the population composed of oscillating droplets, the deformation leads to an increase of the surface of the sinking droplets especially for low magma ocean viscosities where R_{max} is smaller than for large magma ocean viscosities. The total exchange surface in the oscillating case is larger than in the non-oscillating case (by 13 to 43 %) but remains smaller than in the iron rain scenario (by 7 to 37 %). For large magma ocean viscosity (i.e. large viscosity contrasts), the droplets do not oscillate and the exchange surface value is close for both oscillating and non oscillating populations. For low magma ocean viscosities (i.e. small viscosity contrasts), the deformations are so important in the oscillating population that the total surface is close to the surface obtained in the iron rain scenario.

It is to be noted that large metallic drops (with $R > R_{max}$) are allowed in the populations used to obtain Fig. 20. Such large drops are not stable but are likely to exist during the second phase of the fragmentation following an impact that occurs in the shallow magma ocean (Wacheul et al., 2014). Within a deep magma ocean, transient drops with radii $R > R_{max}$ will fragment in smaller droplets and disappear from the populations used in Fig. 20. We can thus redo our calculation by imposing a cut-off at R_{max} using the values from our numerical models (Fig. 14). Fig. 21 illustrates the total potential exchange surface within a sinking cloud of metallic droplets as a function of the magma ocean viscosity considering the same initial volume as in Fig. 20. Imposing a cut-off at R_{max} generates a population of smaller droplets than in Fig. 20. In the oscillating and non oscillating populations used in Fig. 21 many droplets are even smaller than the maximum stable drop radius of the iron rain model. Hence Fig. 21 shows that the total surface of the metallic droplets for both the oscillating and non oscillating populations is larger than the total surface derived from the iron rain scenario. Still, the non oscillating model will be less efficient for thermo-chemical equilibrium than the oscillating model and large magma ocean viscosities (i.e. large viscosity contrasts) significantly reduce (by a factor 10) the potential exchange surface between the silicate and metallic phases.

Results from Figs. 20 and 21 both underline the competition between (1) the deformation processes at the scale of the droplet that enhance the equilibration between the iron and silicate phases and (2) the viscosity contrast that limits the potential exchange surface by allowing large drops. In the shallow part of the magma ocean where large transient metallic drops are likely to exist, the thermo-chemical equilibration will be less efficient than in the deepest part of the magma ocean. However, this conclusion needs to be constrained by implementing thermo-chemical transfers in our dynamical models and using realistic partition coefficients and conductivities that should vary with pressure and temperature.

5. Conclusions and future works

During the late stages of planetary accretion, large impacts between differentiated protoplanets have strongly influenced the thermo-chemical state of the future terrestrial planets. Following the impact and the formation of a deep magma ocean, the metallic phase from the impactor has overcome strong deformation and fragmentation processes before reaching the deepest part of the magma ocean. The dynamics of this fragmentation probably played a key role on the equilibration efficiency between the metallic phase from the impactor and the impacted proto-mantle.

We have performed axisymmetric numerical simulations to model the sinking dynamics of an initially spherical liquid iron drop within a molten silicate phase.

We have explored a large range of relevant parameters, considering initial drop radii in the range of $[1-350]$ mm resulting from the breakup of an initially larger metallic diapir, and magma ocean viscosities in the range $[0.05-100]$ Pa.s. This large range of viscosity is meant to encompass all relevant geophysical situations, depending on pressure, depth, temperature, composition and impact history.

For large Reynolds numbers, we have showed that the drag coefficient for all viscosity ratios converges towards an unique value on the order of 3.5 ± 0.5. We have found that the maximum stable drop radius increases as a function of the magma ocean viscosity following a power law that scales with $\mu_s^{0.32}$. The corresponding critical Weber number increases as a function of the viscosity ratio following two power laws depending on the breakup regime, that scale with $R_\mu^{0.187}$ and $R_\mu^{0.483}$ for the range of low and large magma ocean viscosity respectively. We have identified five breakup mechanisms depending on the Weber and Reynolds numbers and on the viscosity ratio between silicates and iron phases. We have also shown that the initial shape of the metallic drop (spherical, prolate or oblate) strongly influences its subsequent dynamics by modifying its final shape before breakup, its potential exchange surface, and the time and distance before breakup. We have emphasized the effect of the viscosity contrast on the potential exchange surface between the iron phase and the molten surrounding silicates. Indeed, an increase of the viscosity ratio decreases the potential exchange surface between the iron drop and the molten silicates while it increases the time and distance before breakup. We have shown that the dynamical boundary layer thickness increases as a function of the drop radius and the magma ocean viscosity following power law that scales with $R^{0.916}$ and $\mu_s^{0.062}$. Finally, we have implemented our numerical results in a first order model to characterise the ability of an initially 10km metallic diapir to exchange with its surrounding environment while fragmenting. Our dynamical model predicts that potential thermo-chemical equilibration within a fragmenting cloud depends on the depth at which the cloud is fragmenting: thermo-chemical equilibration should be less efficient in the shallowest part of the magma ocean than in the deepest part.

The next step is now to implement in our models the resolution of the equations governing the thermo-chemical exchanges between the metallic phase and the magma ocean. The chemical and thermal diffusion of a sinking undeformable sphere has been extensively studied in the chemical/heat transfer literature (Levich, 1962; Clift et al., 1978). In their numerical models, Ulvrová et al. (2011) evaluated time scales of chemical equilibration within an undeformable metallic droplet sinking through a deformable medium. If the exchange dynamics in the case of a sinking sphere is strongly constrained, the dynamics of thermo-chemical equilibration between a deformable droplet and its environment and the influence of the viscosity contrast between the two phases still deserve extensive studies.

As shown in our study, the depth of the magma ocean could also influence the fragmentation dynamics. As large transient droplets are more likely in the early fragmentation regime, full thermo-chemical equilibration could be achieved deeper in the magma ocean. The transfer parameters governing the equilibration rate are also pressure/temperature dependent. The viscosity of the molten silicates (Karki and Stixrude, 2010), the partition coefficient of lithophile/siredophile elements (Bouhifd and Jephcoat, 2003) and the thermal conductivity of iron (de Koker et al., 2012) are all affected by pressure changes with depth. An exhaustive study accounting for realistic parameters in the context of a deep magma ocean will surely help to constrain the thermo-chemical signature at the end of the core-mantle separation.

Acknowledgements

The authors acknowledge funding by the ERC under the European Union's Horizon 2020 research and innovation program through Grant No. 681835-FLUDYCO-ERC-2015-CoG. This research also received funding from the French PNP program (INSU-CNRS), the French Government Laboratory of Excellence initiative No. ANR-10-LABX-0006 and the Région Auvergne. This paper is Laboratory of Excellence ClerVolc contribution no. XX.

6. Appendix: computational resolution and convergence

In order to confirm that our mesh correctly captures the dynamics of the falling drop within the magma ocean and to determine the quality and limits of our numerical model, we performed systematics tests on two representative cases.

In the first case, we focus on the dynamics of a strongly oscillating drop that does not converge to a single shape and remains in oscillation (simulation #18 in Table 2). This corresponds to a worst case scenario from a numerical point of view. Fig. (22 (left)) shows the normalised boundary layer thickness on the drop radius as a function of different grid sizes $h_x = R/15, R/25, R/33.4, R/40, R/50, R/66.7$. We observe a reasonable convergence of the numerical results from $h_x = R/40$, with changes limited to 1.4%. To quantify the dynamic difference between $h_x = R/40$ and the finest mesh $h_x = R/66.7$, we calculate the normalised exchange surface as a function of time in Fig. (22 (Right)). We note that the first two drop oscillations have the same dynamics; then, differences occur. Yet the dynamical times remain close, and the evolution of the exchange surface is almost the same between the two mesh sizes, with a relative maximum error $\simeq 3.5\%$.

In this paper, we are also interested in the fragmentation modes. To confirm that these fragmentation modes don't depend on the mesh size and don't come from any numerical artifact, we calculate an extremely distorted drop which breaks up after a few oscillations in a second test case (simulation #83 in Table 2). Fig. (23) shows the final drop shape just after the breakup for the grid sizes $h_x = R/40$ and $h_x = R/66.7$. This figure confirms that from $h_x = R/40$, the fragmentation mode and the final drop shape do not change significantly with the grid resolution.

We finally compare the cost (CPU) for one second of simulation of the first test case with different mesh sizes in Table 3. The finest mesh is 4 times more expensive than $h_x = R/40$. The purpose of this article being to perform a systematic study to capture the drop dynamics for a large range of radius and ambient viscosity, we have chosen the mesh size of $h_x = R/40$, which is a good compromise between simulation costs and global dynamical results.

Table 3: Comparison the cost of one simulation for three different grid sizes

Grid size (h_x)	CPU
$R/40$	51h15
$R/50$	121h5
$R/66.7$	205h

References

M. J. Assael, K. Kakosimos, R.M. Banish, J. Brillo, I. Egry, R. Brooks, P.N. Quested, K.C. Mills, A . Nagashima, Y. Sato, and W.A. Wakeham. Reference data for the density and viscosity of liquid aluminum and liquid iron. J. Phys. Chem. Ref. Data, 35:285–300, 2006.

D. Bhaga and M. E. Weber. Bubbles in viscous liquids : shapes, wakes and velocities. Fluid Mech., 105:61–85, 1981.

T. Bonometti and J. Magnaudet. Transition from spherical cap to toroidal bubbles. Phys. Fluids, 18:052102, 2006.

A. Bouhifd, V. Clési, A. Boujibar, N. Bolfan-Casanova, C. Cartier, T. Hammouda, M. Boyet, G. Manthilake, J. Monteux, and D. Andrault. Silicate melts during earth's core formation. Chemical Geology, 461:128–139, 2017.

M. Bouhifd and A. Jephcoat. The effect of pressure on partitioning of ni and co between silicate and iron-rich metal liquids: a diamond-anvil cell study. Earth Planet. Sci. Lett., 209:245255, 2003.

X.K. Cao, Z.G. Sun, W.F. Li, H.F. Liu, and Z.H. Yu. A new breakup regime of liquid drops identified in a continuous and uniform air jet flow. Physics of Fluids, 19:057103, 2007.

J. E. Chambers. Planetary accretion in the inner solar system. Earth Planet. Sci. Lett., 223:241–251, 2004.

R. Clift and W. H. Gauvin. The motion of particles in turbulent gas streams. 1:14–28, 1970.

R. Clift, J. R. Grace, and M. E. Weber. Bubbles, drops and particles. Academic Press, New York, 1978.

T. W. Dahl and J. Stevenson. Turbulent mixing of metal and silicate during planet accretion and interpretation of the hf-w chronometer. Earth Planet. Sci. Lett., 295:177 – 186, 2010.

Z. Dai and G.M. Faeth. Temporal properties of secondary drop breakup in the multimode breakup regime. Multiphase Flow, 27:217 – 236, 2001.

R. C. Darton and D. Harrison. The rise of single gas bubbles in liquid fluidized beds. Transactions of the Institution of Chemical Engineers, 52:301 – 306, 1974.

R. Davies and G. I. Taylor. The mechanics of large bubbles rising through extended liquids and through liquids in tubes. Proc. R. Soc. London 200, 1950.

N. de Koker, G. Steinle-Neumann, and V. Vlček. Electrical resistivity and thermal conductivity of liquid fe alloys at high p and t, and heat flux in earths core. PNAS, 109:4070–4073, 2012.

G.A. de Wijs, G. Kresse, L.Vocadlo, D. Dobson, D.Alfè, M.J. Gillan, and G.D. Price. The viscosity of liquid iron at the physical conditions of the earths core. Nature, 392:805–807, 1998.

R. Deguen, M. Landeau, and P. Olson. Turbulent metal - silicate mixing, fragmentation, and equilibration in magma oceans. Earth Planet. Sci. Lett., 391: 274–287, 2014.

Renaud Deguen, Peter Olson, and Philippe Cardin. Experiments on turbulent metal-silicate mixing in a magma ocean. Earth and Planetary Science Letters, 310(3-4):303–313, 2011.

J.R. Fleck, C.L. Rains, D.S. Weeraratne, C.T. Nguyen, D.M. Brand, S.M. Klein, J.M. McGehee, J.M. Rincon, C. Martinez, and P.L. Olson. Iron diapirs entrain silicates to the core and initiate thermochemical plumes. Nature Communications, 2018.

J. S. Hadamard. Mouvement permanent lent d'une sphere liquide et visqueuse dans un liquide visqueux. C. R. Acad. Sci., 152:17351738, 1911.

J. Han and G. Tryggvason. Secondary breakup of axisymmetric liquid drop. Physics of Fluids, 11, 1999.

J. F. Harper and D. W. Moore. The motion of a spherical liquid drop at high reynolds number. Fluid Mech., 32:367–391, 1968.

W. K. Hartmann and D. R. Davis. Satellite-sized planetesimals and lunar origin. Icarus, 24:504514, 1975.

J. Hu, R. Jia, K.T. Wan, and X. Xiong. Simulation of droplet impingement on a solid surface by the level set method. COMSOL Conference in Boston, 2014.

H. Ichikawa, S. Labrosse, and K. Kurita. Direct numerical simulation of an iron rain in the magma ocean. GEOPHYSICAL RESEARCH, 115:B01404, 2010.

S. I. Karato and V. Rama Murthy. Core formation and chemical equilibrium in the earth physical considerations. Phys. Earth Planet. Int., 100:61–79, 1997.

B. B. Karki and L. P. Stixrude. Viscosity of mgsio3 liquid at earthś mantle conditions : Implications for an early magma ocean. Science, 328:740–742, 2010.

T. Kékesi, G. Amberg, and L. P. Wittberg. Drop deformation and breakup. International Journal of Multiphase Flow, 66:1–10, 2014.

J. D. Kendall and H. Melosh. Differentiated planetesimal impacts in a terrestrial magma ocean: fate of the iron core. Earth Planet. Sci. Lett., 448:2433, 2016.

D. S. Kim, M. Burger, G. Frohlich, and H. Unger. Experimental investigation of hydrodynamic fragmentation of gatliunm drops in water flows. Int. Mtg on Light Water Reactor Severe Accident Evaluation, Cambridge, Mass, 1983.

T. Kleine, C. Münker, K. Mezger, and H. Palme. Rapid accretion and early core formation on asteroids and the terrestrial planets from Hf-W chronometry. Nature, 418:952–955, 2002.

S. A. Krzeczkowski. Measurements of liquid droplet disintegration mechanism. Multiphase Flow, 6:227–239, 1980.

M. Landeau, R. Deguen, and P. Olson. Experiments on the fragmentation of a buoyant liquid volume in another liquid. Fluid Mech., 749:478518, 2014.

V. Levich. Physicochemical hydrodynamics. 1962.

E. Loth. Quasi-steady shape and drag of deformable bubbles and drops. Multiphase flow, 34:523546, 2008.

X-Y. Luo, M-J. Ni, A. Ying, and M. Abdou. Application of the level set method for multi-phase flow computation in fusion engineering. Fusion Engineering and Design, 81:15211526, 2006.

R. Mei, J. F. Klausner, and C. J. Lawrence. A note on the history force on a spherical bubble at finite reynolds number. Phys. Fluid, 6:418 – 420, 1994.

J. Monteux and J. Arkani-Hamed. Consequences of giant impacts in early Mars: Core merging and Martian dynamo evolution. J. Geophys. Res. (Planets), 119: 480–505, 2014. doi: 10.1016/j.icarus.2013.05.008.

J. Monteux, N. Coltice, F. Dubuffet, and Y. Ricard. Thermo-mechanical adjustment after impacts during planetary growth. Geophys. Res. Lett., 34: 24201–24205, 2007.

J. Monteux, Y. Ricard, N. Coltice, F. Dubuffet, and M. Ulvrova. A model of metal-silicate separation on growing planets. Earth and Planetary Science Letters, 287:353–362, October 2009. doi: 10.1016/j.epsl.2009.08.020.

D. W. Moore. The velocity of rise of distorted gas bubbles in a liquid of small viscosity. Fluid Mech., 23:749 – 765, 1965.

A. Morbidelli, J.I. Lunine, D.P. O'Brien, S.N. Raymond, and K.J. Walsh. Building terrestrial planets. Earth Planet. Sci., 40:451 – 475, 2012.

David P. O'Brien, Alessandro Morbidelli, and Harold F. Levison. Terrestrial planet formation with strong dynamical friction. icarus, 184:39–58, September 2006. doi: 10.1016/j.icarus.2006.04.005.

M. Ohta and M. Sussman. The buoyancy-driven motion of a single skirted bubble or drop rising through a viscous liquid. Phys. Fluids, 24:112101, 2012.

M. Ohta, Y. Akama, Y. Yoshida, and M. Sussman. Three-dimensional simulations of vortex ring formation from falling drops in an immiscible viscous liquid. Chem. Engng Japan, 42:648655, 2009.

M. Ohta, S. Yamaguchi, Y. Yoshida, and M. Sussman. The sensitivity of drop motion due to the density and viscosity ratio. Phys. Fluids, 22:072102, 2010.

M. Ohta, Y. Akama, Y. Yoshida, and M. Sussman. Inuence of the viscosity ratio on drop dynamics and breakup for a drop rising in an immiscible low-viscosity liquid. Fluid Mech., 752:383409, 2014.

P. D. Patel. Hydrodynamic fragmentation of drops. Ph.D. Dissertation, Purdue Univ.. West Lafayette, Ind., 1978.

P. D. Patel and T. G. Theofanous. Hydrodynamic fragmentation of drops. Fluid Mech., 103:207223, 1981.

M. Pilch and C. A. Erdman. Use of breakup time data and velocity history data to predict the maximum size of stable fragments for acceleration-induced breakup of a liquid drop. Multiphase Flow, 13:741757, 1987.

J.P. Poirier. Transport properties of liquid metals and viscosity of the earths core. Geophysical Journal, 92:99105, 1988.

D. C. Rubie, H. J. Melosh, J. E. Reid, C. Liebske, and K. Righter. Mechanisms of metal-silicate equilibration in the terrestrial magma ocean. Earth and Planet. Sci. Lett., 205:239–255, January 2003.

H. Samuel. A re-evaluation of metal diapir breakup and equilibration in terrestrial magma oceans. Earth Planet. Sci. Lett., 313-314:105–114, 2012.

D. J. Stevenson. fluid dynamics of core formation. Origin of the Earth, pages 231–249, 1990.

W. B. Tonks and H.J. Melosh. Core formation by giant impacts. ICARUS, 100: 326–346, 1992.

M. Touboul, T. Kleine, B. Bourdon, H. Palme, and R. Wieler. Late formation and prolonged differentiation of the Moon inferred from W isotopes in lunar metals. Nature, 450:1206–1209, 2007.

M. K. Tripathi, K. C. Sahu, and R. Govindarajan. Dynamics of an initially spherical bubble rising in quiescent liquid. Nature communications, 2015.

M. Ulvrová, N. Coltice, Y. Ricard, S. Labrosse, and F. Dubuffet Velìmskỳand M. Šràmek. Compositional and thermal equilibration of particles, drops, and diapirs in geophysical flows. Geochem. Geophys. Geosyst, 12, 2011.

E. Villermaux and B. Bossa. Single - drop fragmentation determines size distribution of rain drops. Nat. Phys., 5:697702, 2009.

J. B. Wacheul and M. Le Bars. Experiments on fragmentation and thermo-chemical exchanges during planetary core formation. Phys. Earth Planet. Int., 276:134 144, 2018.

J. B. Wacheul, M. LeBars, J. Monteux, and J. M. Aurnou. Laboratory experiments on the breakup of liquid metal diapirs. Earth Planet. Sci. Lett., 403: 236245, 2014.

M. J. Walter and R. G. Tronnes. Early earth differentiation. Earth Planet. Sci. Lett., 225:253 269, 2004.

B.J. Wood, M.J. Walter, and J. Wade. Accretion of the earth and segregation of its core. Nature, 441:825 833, 2006.

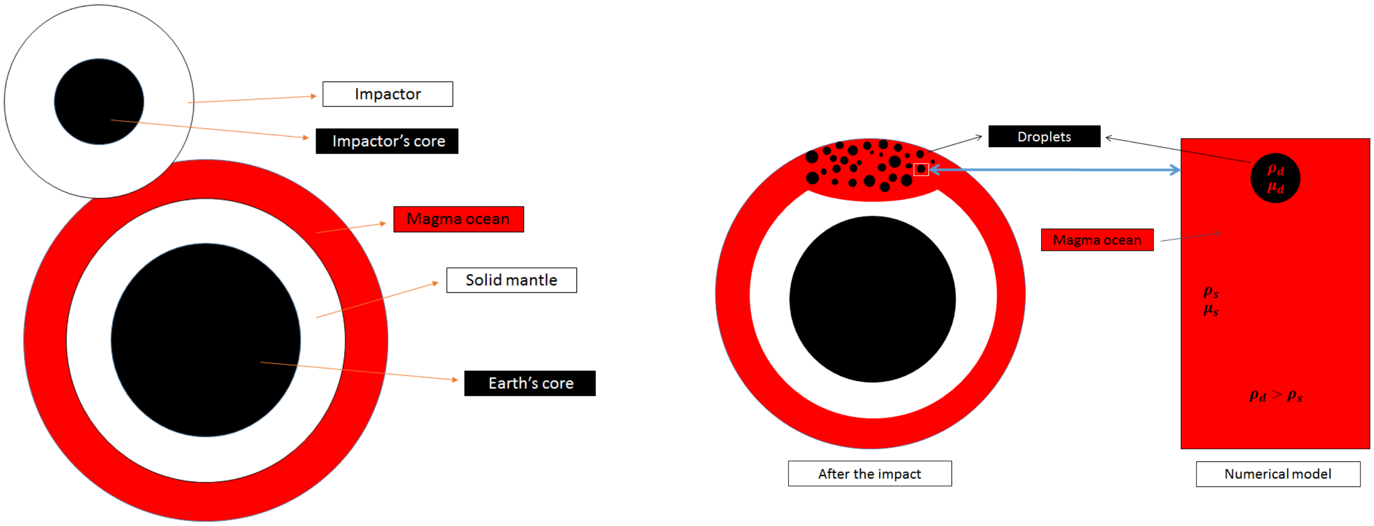

Figure 1: Schematic of the metal/silicate separation during an impact between a differentiated planetesimal and the early Earth with a schematic of our computational domain.

.

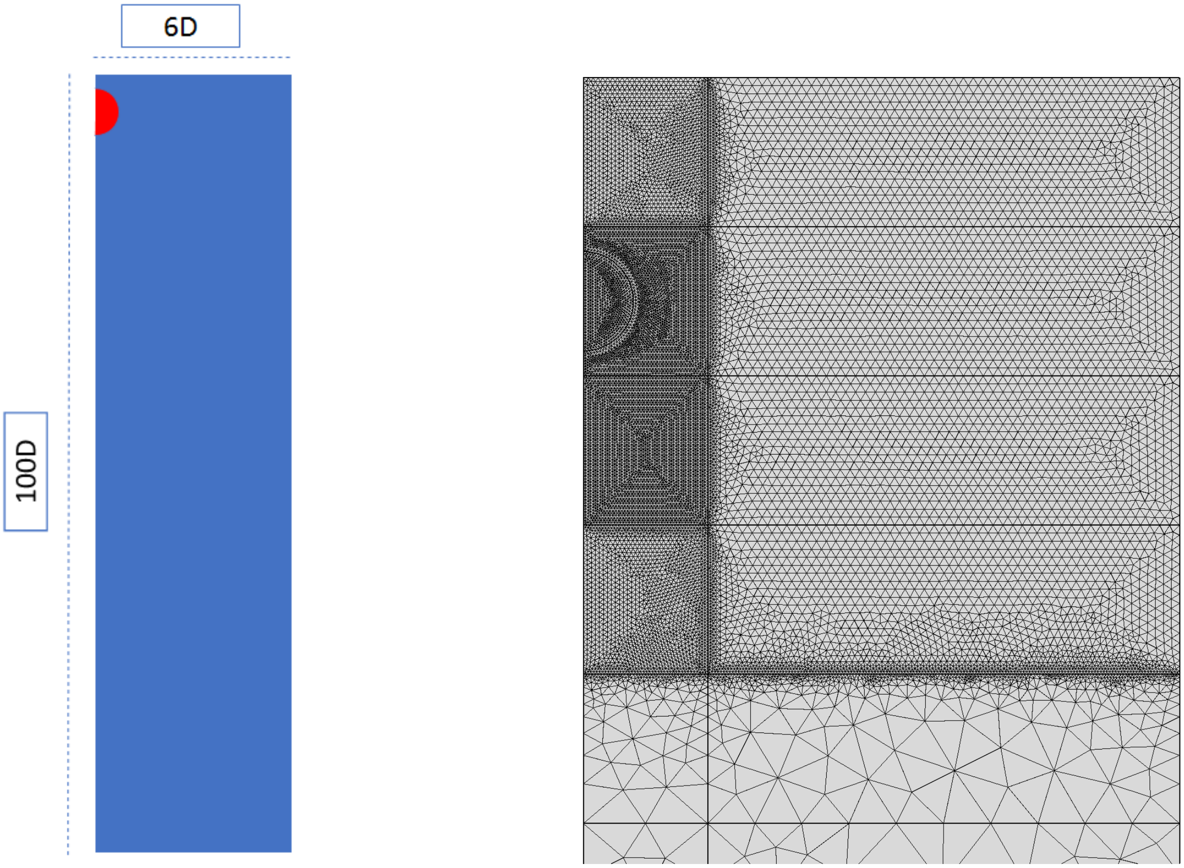

Figure 2: Global view of our geometry with the initial drop at the top (left), and a zoom illustrating our manual method for adaptive mesh (right).

.

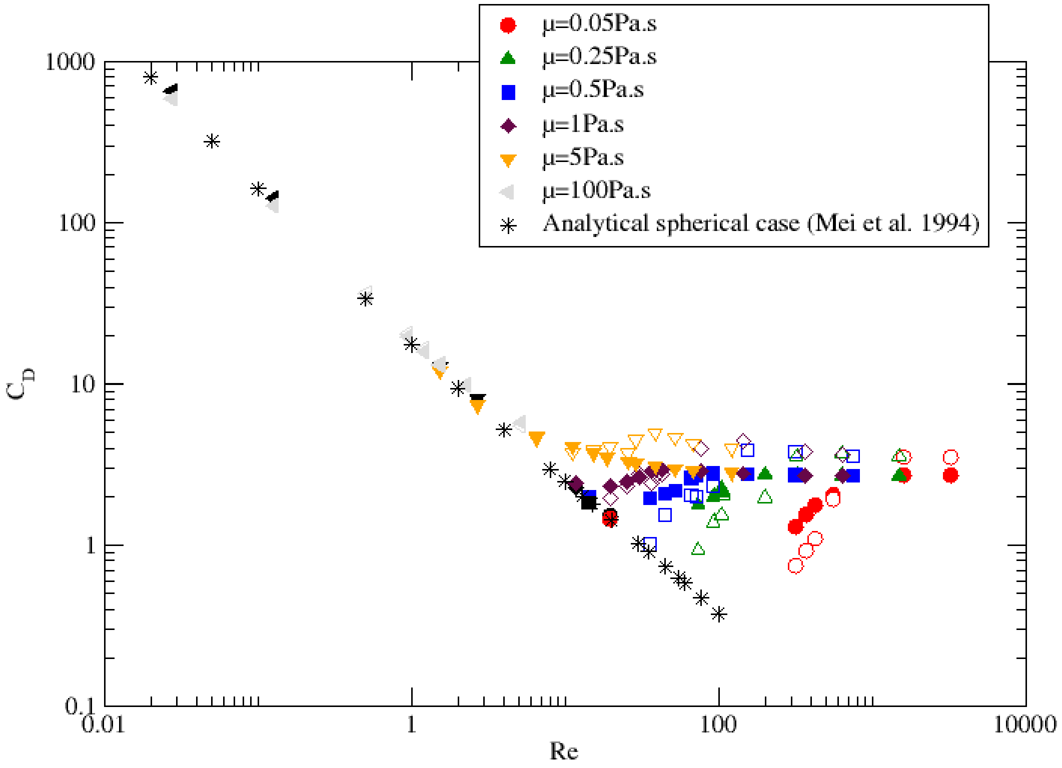

Figure 3: Drag coefficient as a function of the Reynolds number for various values of the silicates viscosity. Filled symbols are the analytical results given by Eq.12, while empty symbols show our numerical results from the first 62 simulations in table 2. Filled black symbols show numerical results for an undeformable sphere $R_\mu = 0$, and black stars are the analytical results from Eq. 10.

.

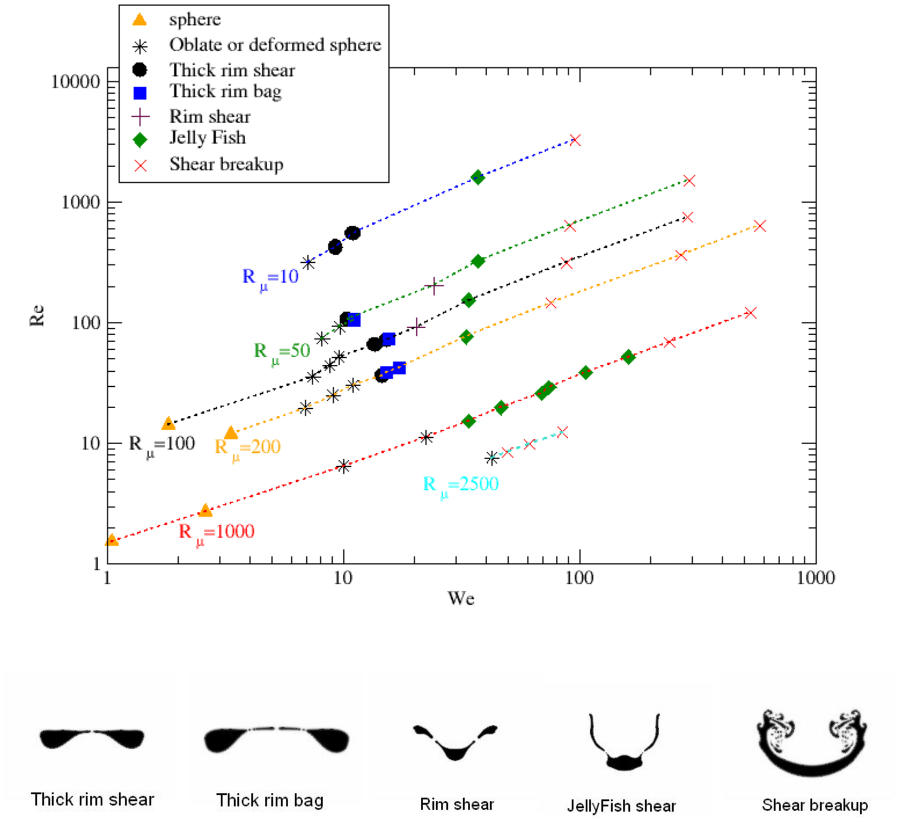

Figure 4: Regime diagram of the fragmentation modes as a function of Re and We numbers for various viscosity ratios: $R_\mu = 10$ (blue dotted line), $R_\mu = 50$ (green dotted line), $R_\mu = 100$ (black dotted line), $R_\mu = 200$ (orange dotted line), $R_\mu = 1000$ (red dotted line), and $R_\mu = 2500$ (turquoise dotted line). Our numerical results come from the first 62 simulations in table 2.

.

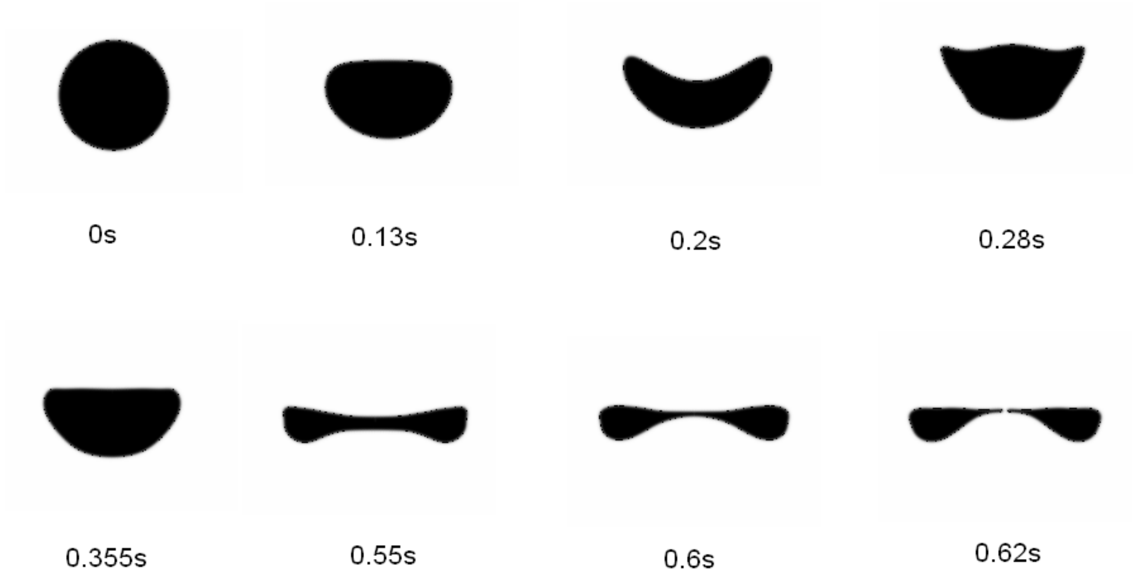

Figure 5: Deformation and thick rim shear breakup of an iron drop within a magma ocean. In this model, $Re = 36.4$, $We = 14.6$, $R_{\mu} = 200$ (simulation #30 in Table 2).

.

Figure 6: Deformation and thick rim bag breakup of an iron drop within a magma ocean. In this model, $Re = 42.5$, $We = 17.2$, $R_\mu = 200$ (simulation #32 in Table 2).

.

Figure 7: Deformation and rim shear breakup of an iron drop within a magma ocean. In this model, $Re = 92.4$, $We = 20.3$, $R_\mu = 100$ (simulation #22 in Table 2).

.

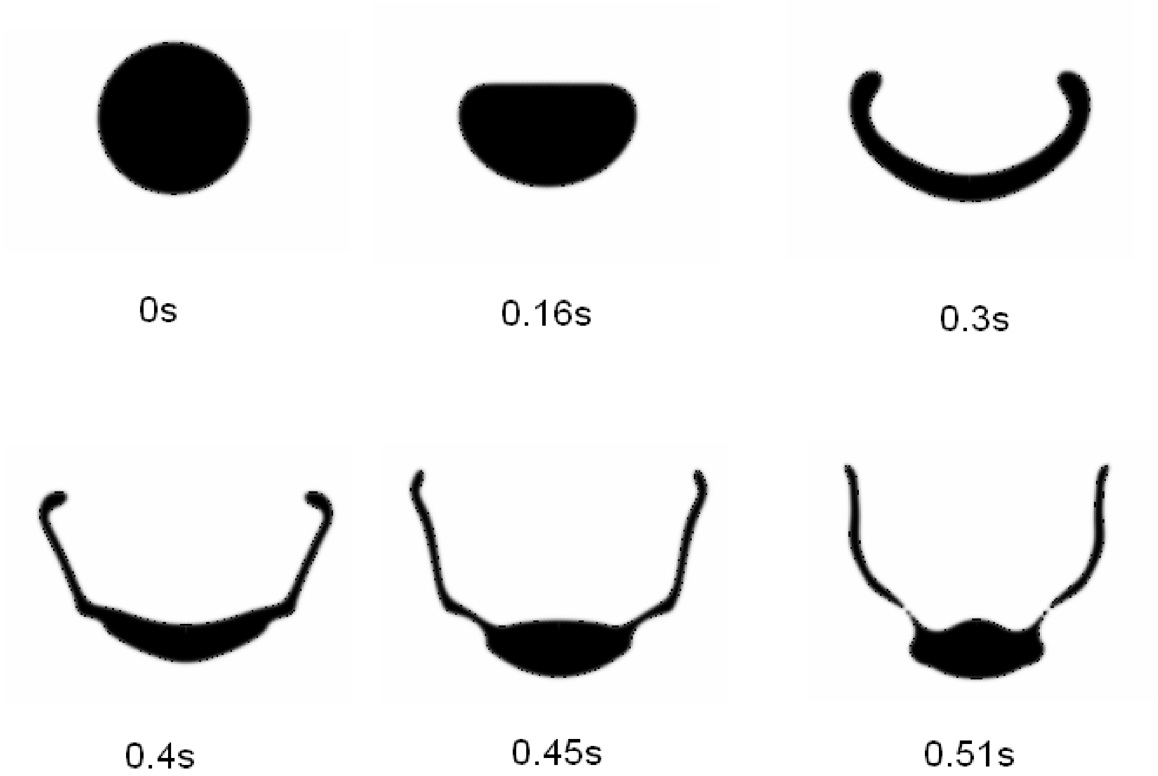

0s 0.16s 0.3s

0.4s 0.45s 0.51s

Figure 8: Deformation and jellyfish shear breakup of an iron drop within a magma ocean. In this model, $Re = 76.1$, $We = 33.1$, $R_\mu = 200$ (simulation #33 in Table 2).

.

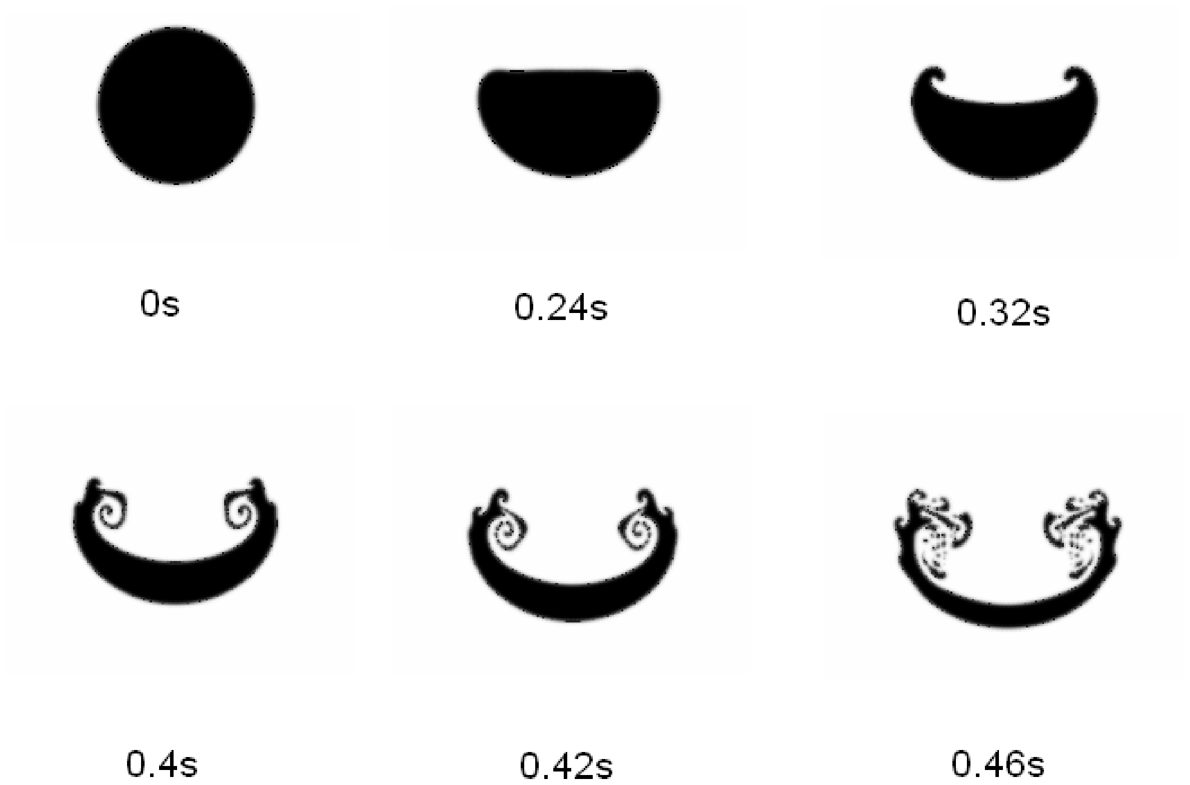

Figure 9: Deformation and shear breakup of an iron drop within a magma ocean. In this model, $Re = 2670$, $We = 636$, $R_\mu = 50$ (simulation #62 in Table 2).

.

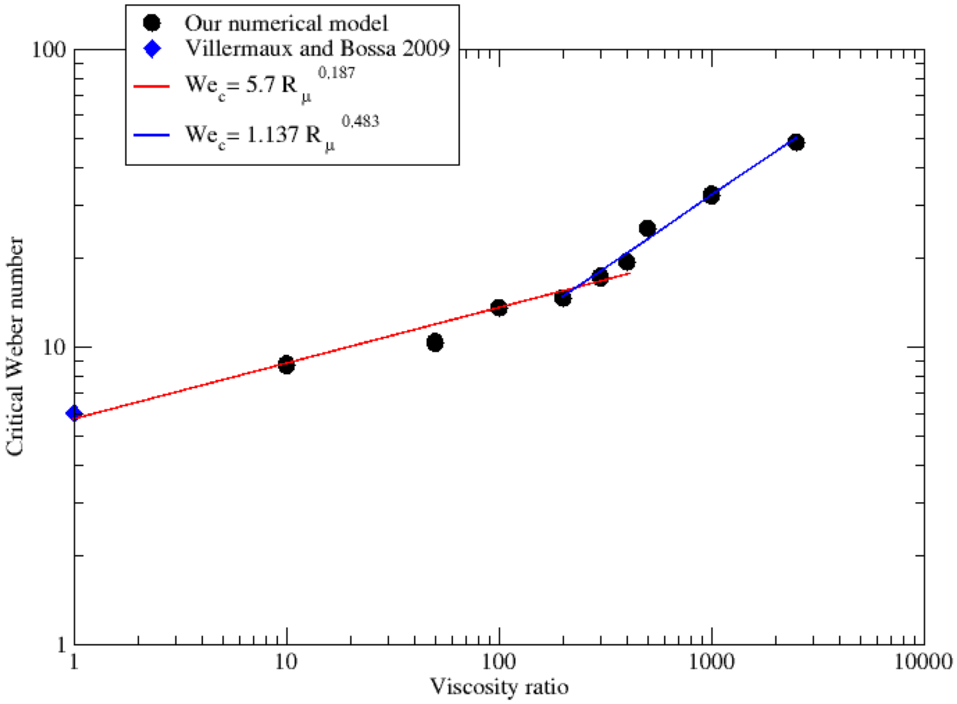

Figure 10: Critical Weber number as a function of the viscosity ratio. The blue diamond is the critical Weber number when the viscosity ratio equal to 1, as obtained by Villermaux and Bossa (2009). The red and blue lines represent the scaling laws derived from our data.

.

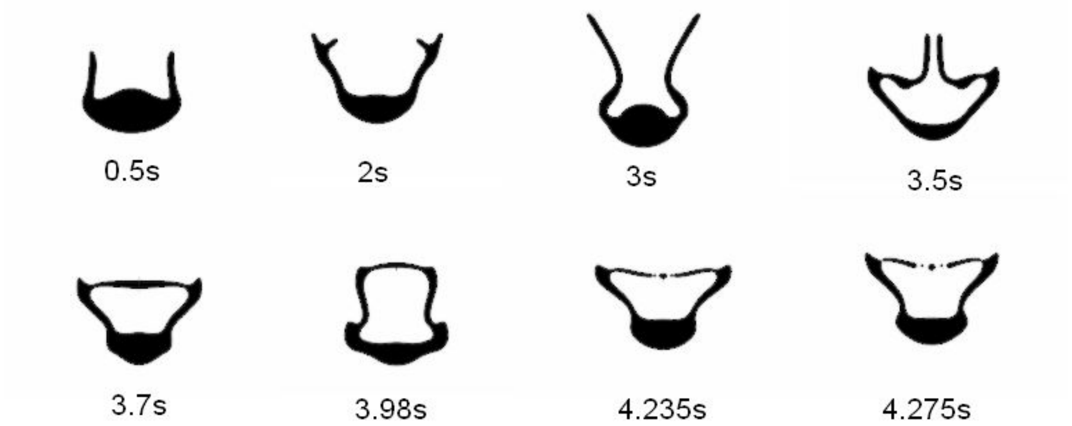

Figure 11: The path of a new fragmentation mode where the iron structure encloses the silicates.

.

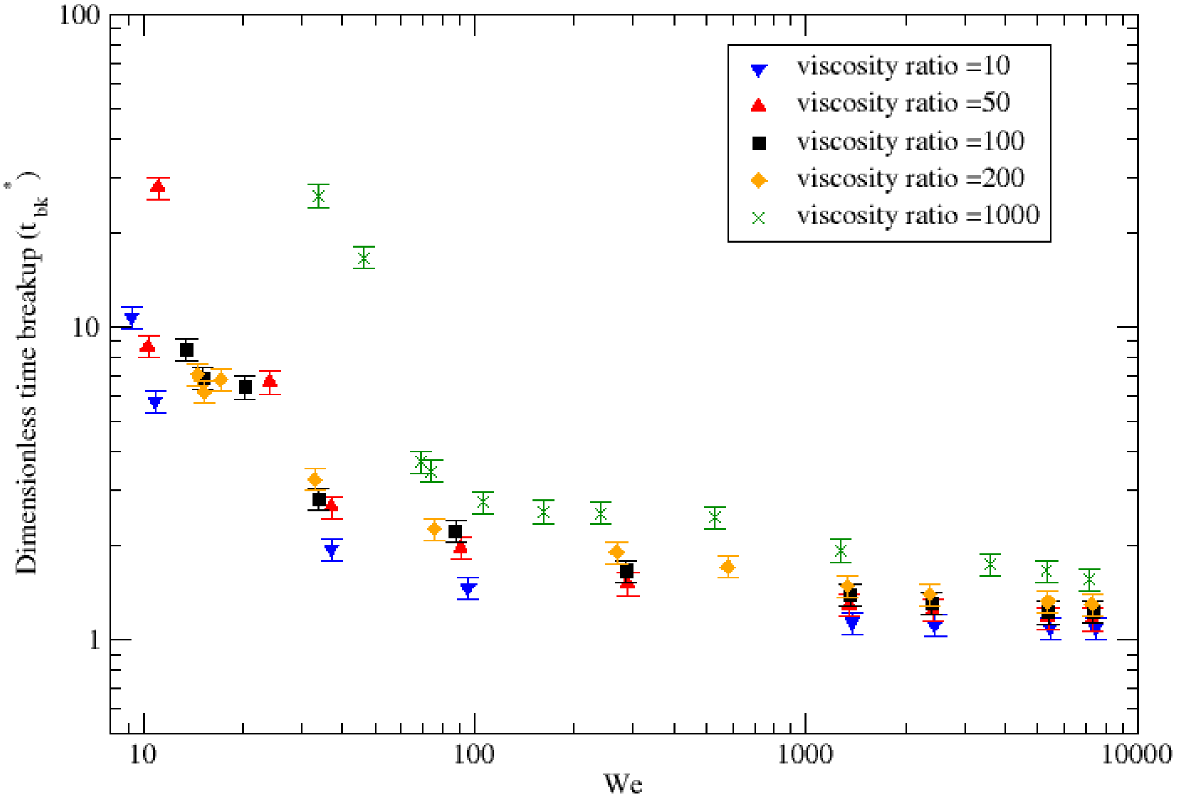

Figure 12: Non-dimensional break-up time as a function of Weber number for viscosity ratios R_μ ranging between 10 and 1000.

.

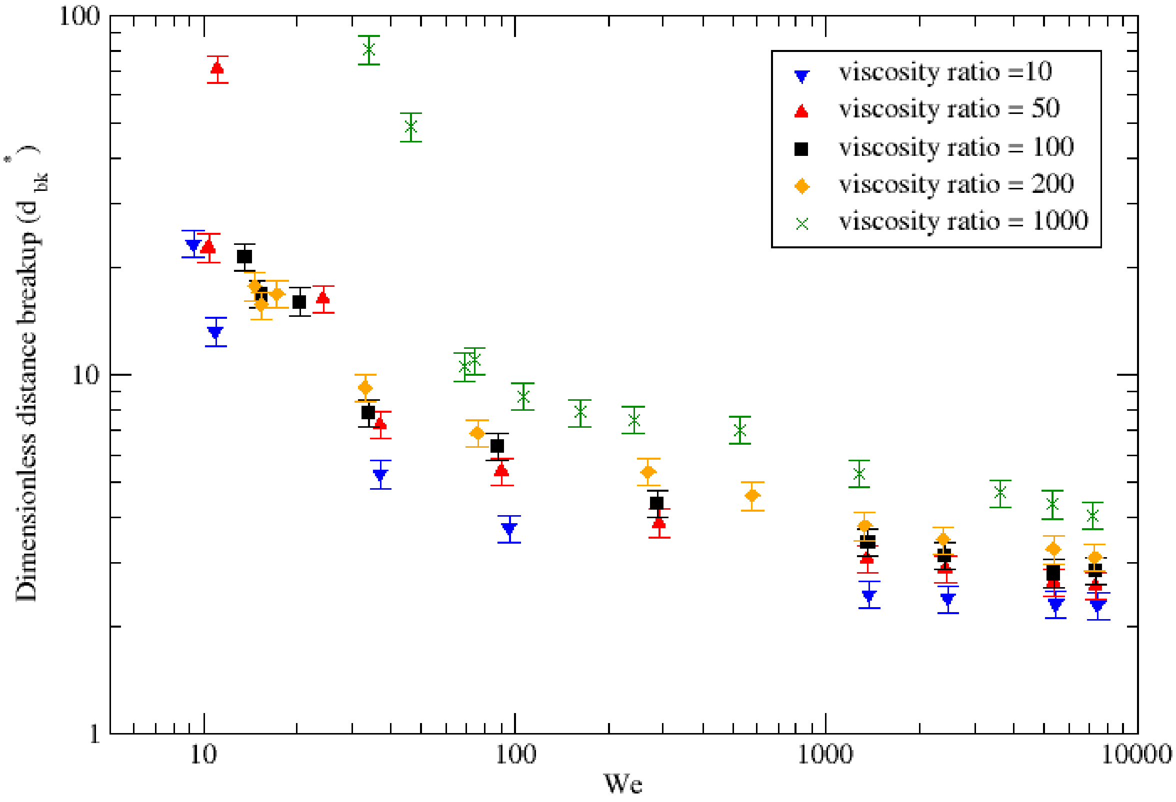

Figure 13: Non-dimensional break-up distance d^*_{bk} as a function of the Weber number for viscosity ratios R_μ ranging between 10 and 1000.

.

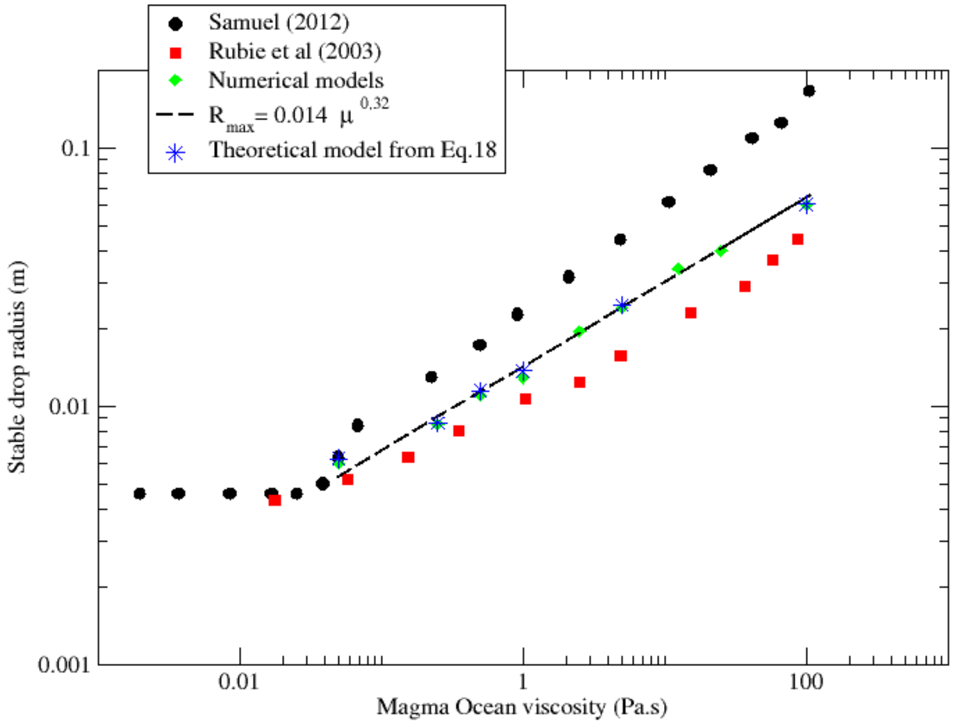

Figure 14: Stable drop radius as a function of plausible magma ocean viscosities. The green diamonds present our numerical results, the red squares correspond to the results of Rubie et al. (2003), the black circles display the results of Samuel (2012), the blue stars correspond the analytical results of the Eq. 18 and the black dash line presents the scaling law proposed by this study.

.

Figure 15: The final shape of the iron droplets for different initial conditions. Spherical case (left), prolate form (middle) and oblate form (right).

.

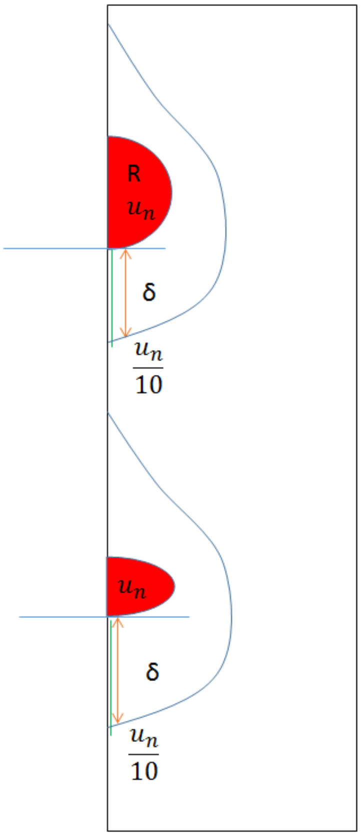

Figure 16: Schematic representation of the geometry used for the determination of the boundary layer thickness δ at the drop surface: spherical case (top) and deformed drop (bottom).

.

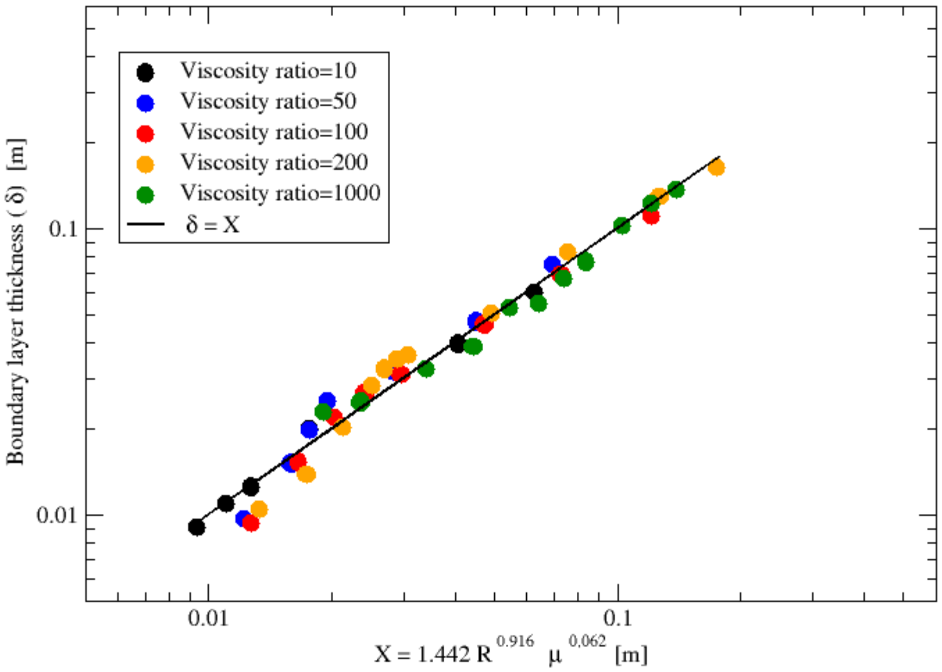

Figure 17: Boundary layer thickness as a function of the varied parameters in this study (drop radius and magma ocean viscosity) for viscosity ratios R_μ ranging between 10 and 1000. Our numerical results come from the first 62 simulations in Table 2).

.

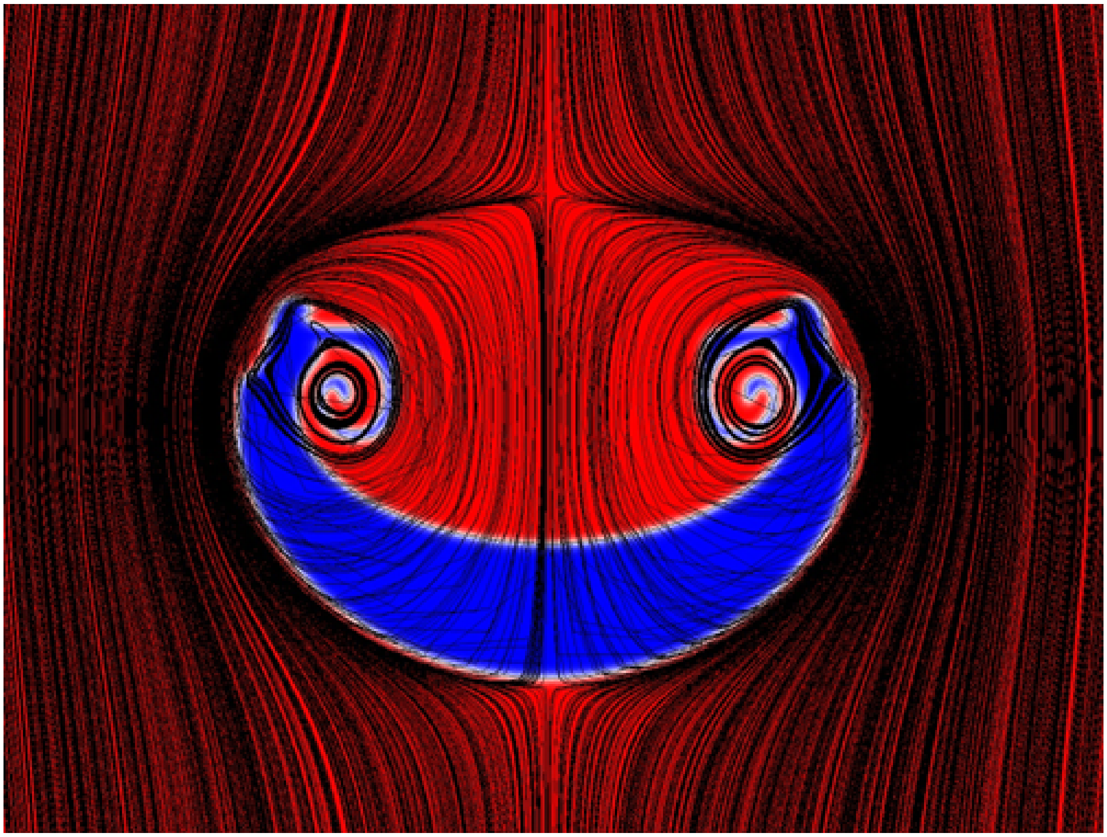

Figure 18: The streamlines around a large drop. In this model, $Re = 2670$, $We = 636$, $R_\mu = 50$ (simulation #62 in Table 2). The black lines are the streamlines, the red region represents the molten silicates and the blue region represents the deformable iron drop.

.

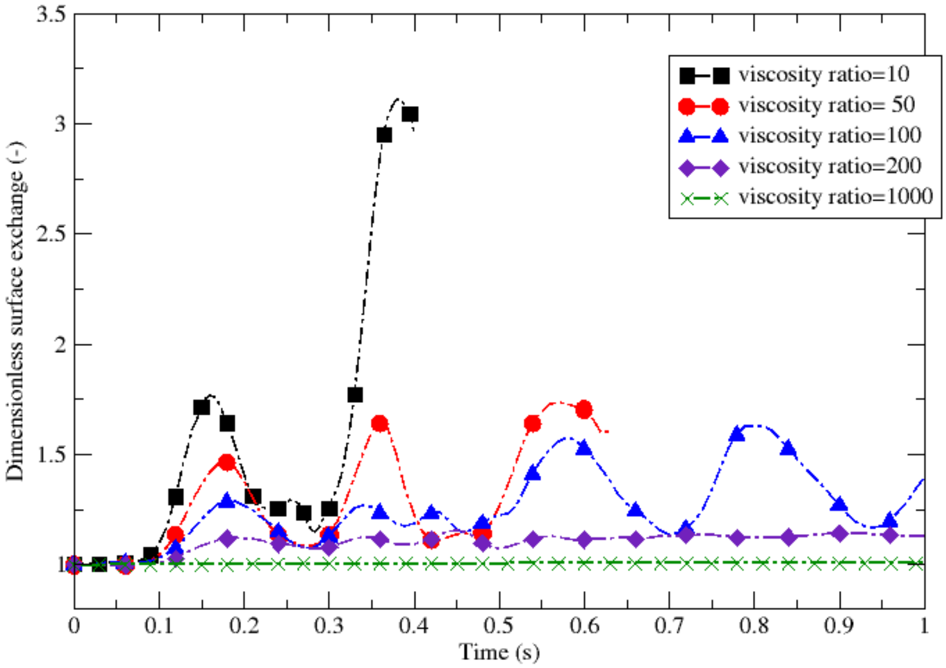

Figure 19: Non-dimensional surface exchange as a function of time for viscosity ratios R_μ ranging between 10 and 1000. Here, we consider a drop of initial radius $R = 10$ mm. For viscosity ratio = 10 (black line), $Re = 553$ and $We = 10.9$. For viscosity ratio = 50 (red line), $Re = 108$ and $We = 10.4$. For viscosity ratio = 100 (blue line), $Re = 44.2$ and $We = 8.74$. For viscosity ratio = 200 (purple line), $Re = 25.1$ and $We = 9.02$. For viscosity ratio = 1000 (green line), $Re = 2.70$ and $We = 2.61$.

.

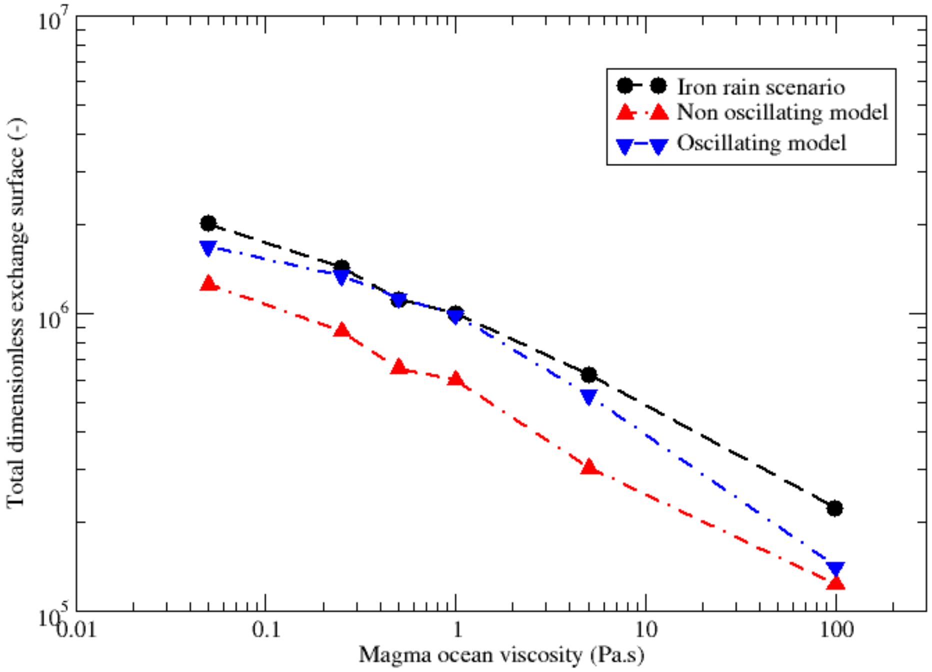

Figure 20: Normalised exchange surface S^* as a function of magma ocean viscosity after the breakup of a 10 km metal diapir. In the sinking droplet population, no cut-off is considered at $R = R_{max}$.

.

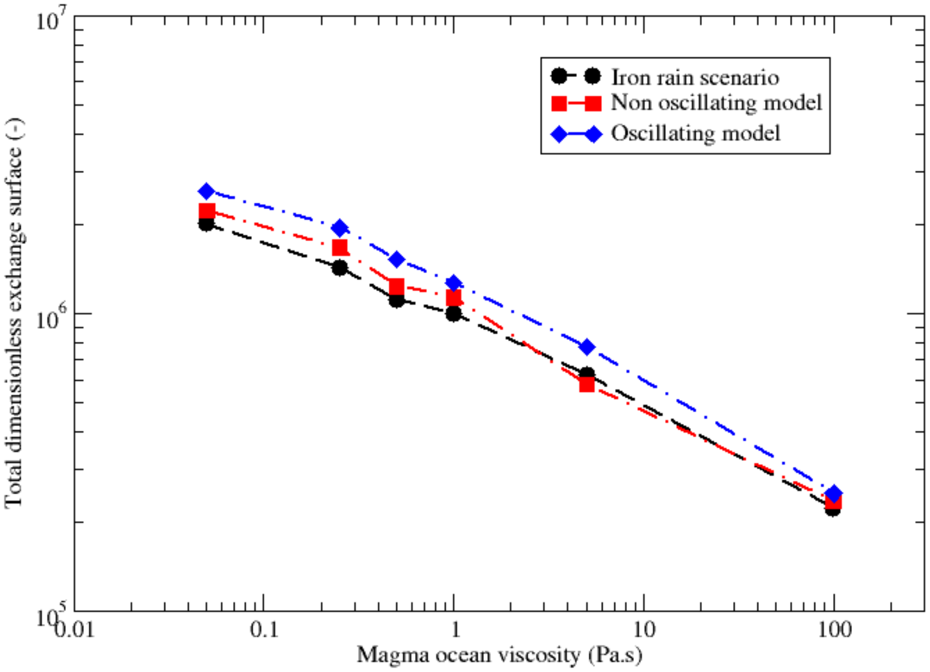

Figure 21: Normalised exchange surface S^* as a function of magma ocean viscosity after the breakup of a 10 km metal diapir. In the sinking droplet population, a cut-off is considered at $R = R_{max}$.

.

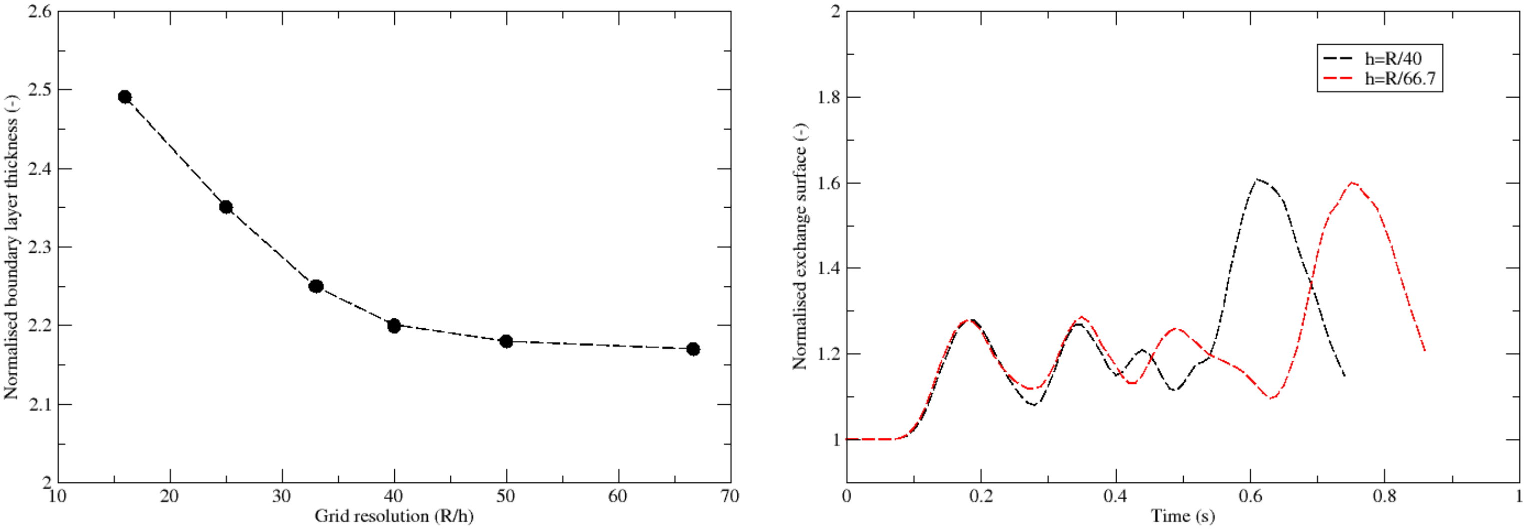

Figure 22: Comparison of different mesh sizes of a strongly oscillating drop (simulation #18 in Table 2). Left: Normalised boundary layer thickness as a function of grid sizes. Right: Normalised exchange surface as a function of time.

.

Figure 23: Comparison of the final shape of the fragmented drop for two different mesh sizes. (simulation #83 in Table 2).

.